PREPRINT NOTICE

This is the author's accepted manuscript of a Letter published in *Environmental Research Letters*: Jing J 2026 *Environ. Res. Lett.* **21** 204030. Accepted 28 September 2026; published 4 November 2026. It has been peer reviewed and includes the corrections made at the proof stage, but it has not been copy-edited or typeset by the publisher. The version of record is available open access at https://doi.org/10.1088/1748-9326/aead02.

Author: Jiawei Jing (Makuhari Development Corporation, Chiba, Japan; jiawei.jing@mkhr.co.jp; ORCID 0009-0000-8365-367X)

Code and derived data: https://doi.org/10.5281/zenodo.23083016

Satellite observations and energy balance constrain the thermal footprint of a hyperscale data-centre cluster

Jiawei Jing

Makuhari Development Corporation, Chiba, Japan

E-mail: jiawei.jing@mkhr.co.jp — ORCID: 0009-0000-8365-367X (corresponding author)

Funding: This research received no external funding.

Abstract

Whether hyperscale data centres (DCs) warm their surroundings divides current evidence: a coarse-resolution satellite preprint attributes ~2 °C of land-surface-temperature (LST) warming to facilities worldwide (Marinoni et al 2026), while peer-reviewed transects near Phoenix measure +0.7-0.9 °C of near-ground air warming a few hundred metres downwind (Sailor et al 2026). Prospective anthropogenic-heat models remain untested against long-term observations, and no major DC market assesses local temperature impact before construction. We provide the first ex-post, controlled satellite test for Japan's largest DC concentration, the Inzai and Tama clusters near Tokyo, whose staggered build-out (twelve facilities, 2011-2025) yields a three-phase event study with replication. The test combines daytime Landsat (2013-2026), 70 m day/night ECOSTRESS and 1 km MODIS with matched pre-2013 controls, facility-level energy disclosures and minimum-detectable-effect analysis, gated by an air-temperature energy-balance ceiling (~0.35 °C, cluster scale, night) that bounds LST a fortiori. Commissioning *cools* the daytime LST by 1.8-2.2 °C — significant under all three reference types, a radiative-property signal opposite in sign to the viral claim. Deep-night facility-scale LST changes are indistinguishable from zero (bounded below ~0.6-1.2 °C), and the cluster-scale night LST bound (0.24-0.29 °C, autocorrelation-corrected, two platforms) closes beneath the air-temperature ceiling. The exclusion of warming at the claimed magnitude rests primarily on energy balance — +2 °C, even in air, would require 6-43 times the available waste heat — with observations supplying consistent bounds at every scale they resolve. Arid- and continental-climate consistency checks (Phoenix and DeKalb)

reproduce the decomposition: in both, night surface warming is largely in place during construction — before any server load — and matches neighbouring non-DC development; conversion, not exhaust. Near-source air warming is real where rejection density is high and climates dry; kilometre-scale surface warming from waste heat is unattainable. The protocol is the ex-post verification tool siting regimes lack.

Keywords: data centres; land surface temperature; anthropogenic heat; urban climate; quasi-experiment; ECOSTRESS

1. Introduction

The siting of hyperscale data centres — whose electricity use is roughly 1.5% of global supply and rising steeply (Masanet et al 2020, IEA 2024), with United States consumption alone projected to reach ~12% of national supply by 2030 (Shehabi et al 2025) — has become a contested environmental-policy question, and their heat impact is now the subject of directly conflicting claims. A widely publicised, not yet peer-reviewed preprint analysing coarse-resolution satellite land surface temperature (LST) around thousands of facilities reports mean local LST warming of +2.07 °C (range 0.3-9.1 °C), decaying out to ~10 km, with heat-exposure claims for roughly 340 million people (Marinoni et al 2026); an immediate physical objection: available waste heat supplies ~1-3% of the required forcing (Masley 2026). Meanwhile the first peer-reviewed field measurements, vehicle transects around four air-cooled facilities in arid Phoenix, find real but localised near-ground *air* warming of +0.7-0.9 °C (peak 2.2 °C), confined to a few hundred metres downwind (Sailor et al 2026).

Three gaps make this dispute unresolvable with existing evidence. First, the modelling literature is prospective only: scaling analyses of anthropogenic-heat impacts (Khanh et al 2025) and mesoscale simulations of concentrated air-conditioning exhaust — night-dominated air warming up to ~0.6 K (Jin et al 2020) — predict tenths of a degree at these fluxes, but no such prediction has been tested against long-term observations around an actual facility, a validation gap the Phoenix team itself highlights. Second, the observational claims lack controls: neither coarse-pixel before/after contrasts nor downwind transects separate waste heat from the land-cover conversion accompanying any large construction project. Third, regulation provides no answer: none of the major DC markets — Singapore, Ireland, the Netherlands, the United States, China, Japan — requires, at the national permitting level, assessing local temperature impact before a data centre is built; heat enters permitting only as a recoverable resource, a noise proxy or an efficiency metric. What waste heat does to a neighbourhood's temperature is predicted by unvalidated models, contested by uncontrolled observations, and assessed by no one.

This Letter closes the first gap and speaks to the other two. Data centres are among the few point sources injecting hundreds of megawatts of heat directly into an inland boundary layer (coastal power stations discharge mostly to the sea or to the sky as latent heat) — a clean natural experiment. We exploit Japan's largest DC concentration — the Inzai/Shirai cluster in Chiba and a replication cluster in Tama, twelve facilities commissioned 2011-2025 (table 1) — with the four elements the dispute has lacked: facility-resolving resolution (70-100 m); day/night separation (daytime LST is dominated by surface radiative properties, so waste heat, if visible, appears at night); matched controls and a three-

phase event design separating commissioning from land-cover conversion; and an explicit minimum-detectable-effect (MDE) statement, without which a non-detection is uninformative. Our contributions: (i) the first ex-post, controlled satellite test of DC waste-heat impact, yielding physically self-consistent bounds; (ii) a mechanistic decomposition of the LST signal into surface radiative-property and anthropogenic-heat components — commissioning *cools* the daytime surface; and (iii) a cross-climate energy-balance framework under which the Phoenix detections and our bounds are two predictions of the same physics.

Because both the physics and the observable quantity change with scale, we distinguish four spatial scales throughout: the *near field* (≤~500 m, where plume-induced 2 m air warming is measurable by ground traverse; Sailor et al 2026); the *facility scale* (70-100 m, LST pixels resolving one building); the *cluster scale* (1-3 km, our MODIS window and the neighbourhoods hosting these facilities); and the *mesoscale* (>10 km, the coarse-pixel warming claims; Marinoni et al 2026). Much of the apparent conflict in the literature dissolves once each result is pinned to its rung.

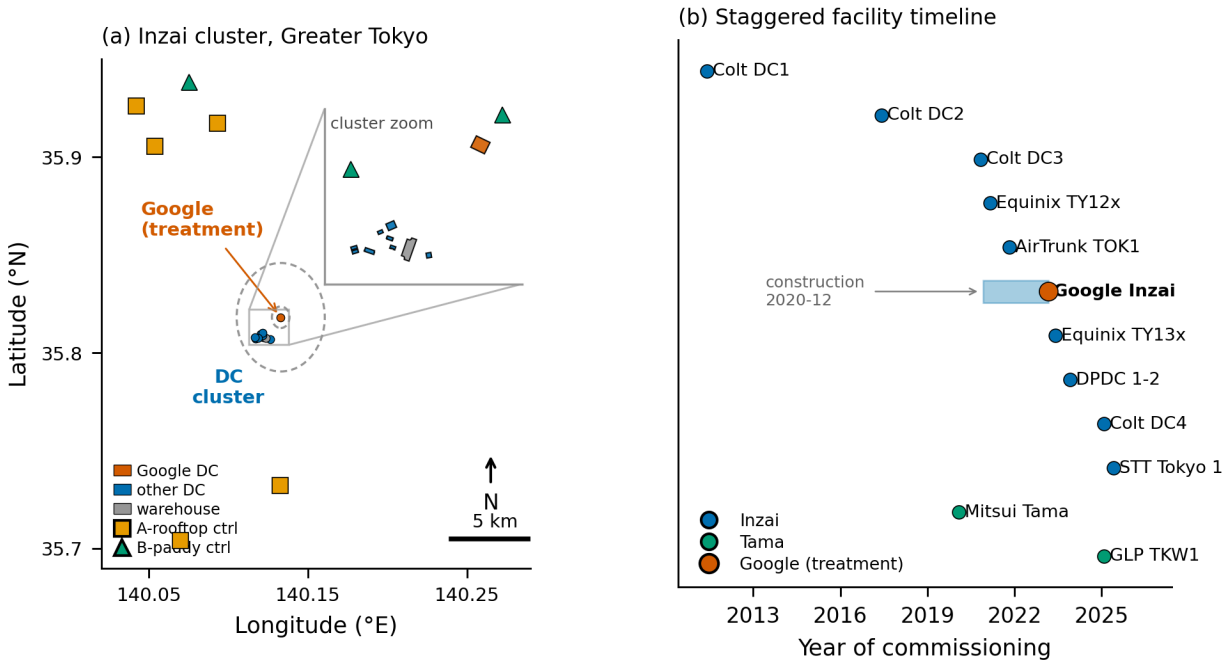


Figure 1. Study area and natural experiment. (a) Inzai cluster, Greater Tokyo: treatment footprint (primary case), other data centres, warehouse, and matched control zones (A: pre-2013 built-up rooftops; B: stable paddy); inset zooms the DC cluster. (b) Staggered commissioning timeline of the twelve facilities, 2011-2025; the primary case shows its construction-to-service span (2020-12 to 2023-03).

2. Study area, natural experiment and regulatory setting

The Inzai cluster (35.81° N, 140.13° E), ~35 km east of central Tokyo on the Shimousa upland, hosts the largest concentration of hyperscale DCs in Japan, amid paddy, cropland, housing and logistics estates. Facility-level disclosures under Japan's mandatory greenhouse-gas scheme (SHK; MOE 2024) give a cluster electricity draw of at least ~126 MW in FY2023 — a strict lower bound, because operators purchasing zero-emission menus report near-zero CO2 while their physical load, and hence waste heat, is unchanged (section 3.4).

The primary facility is itself embedded in coordinated fringe redevelopment: one parcel of the ~50 ha Goodman Business Park, a seven-stage master-planned logistics-and-DC hub built on former woodland and cropland from 2016 onward, its warehouse roofs carrying a ~15 MW photovoltaic array. Facility-scale attribution in such a landscape requires footprint-resolving resolution and non-local controls — the constraint that drives section 3.2.

The cluster's heat-rejection technology is mixed and only partially disclosed: the primary operator reports elevated-temperature operation with seasonal free cooling, the largest colocation campus advertises direct-air free cooling (design PUE 1.15), and the rest do not disclose. For section 3.4 the heterogeneity is immaterial by construction: we assume the entire load is rejected as sensible heat, the assumption that maximises predicted warming; any evaporative fraction only lowers the ceilings.

The regulatory setting makes the cluster genuinely untested. Data centres fall outside Japan's national EIA law and the Factory Location Act; the Inzai facilities were permitted through ordinary building confirmation, with no environmental assessment on record. Even a comparable Greater-Tokyo development that did undergo prefectural EIA (triggered by land-development scale, not data-centre status) contained no quantitative prediction of exhaust-heat effects. No ex-ante thermal prediction exists for these facilities — only the ex-post record constructed here.

Twelve facilities with public dates form the staggered build-out (table 1, figure 1). We are explicit about what the design provides. One facility — the primary case (99,600 m² gross floor area; construction December 2020, in service March 2023) — cleanly partitions the record into pre/construction/operation phases with multi-year pre-baselines in all sensors. The Tama cluster provides independent replication (one facility commissioned 2020-02 with full Landsat pre/post, plus a pre-2013 legacy DC as an always-on placebo). The remaining facilities enter cluster-scale aggregates only.

Table 1. Facilities in the staggered build-out (IT capacity where disclosed; floor area otherwise; sources: operator press releases and industry publications).

Cluster	Facility	Construction	In service	Scale
Inzai	Colt Inzai DC1	—	2011	8 MW
Inzai	Colt Inzai DC2	—	2017	n/d
Inzai	Colt Inzai DC3	—	2020-11	27 MW
Inzai	Equinix TY12x	—	2021-03	~54 MW (final)
Inzai	AirTrunk TOK1	—	2021-11	60 MW+ (300 MW planned)
Inzai	Primary case (Google Inzai)	2020-12	2023-03	99,600 m² GFA
Inzai	Equinix TY13x	—	2023-06	8 MW (36 MW final)
Inzai	DPDC Inzai Park 1-2	2020-10	~2023-12	31,400 m² GFA
Inzai	Colt Inzai DC4	—	2025-02	20 MW
Inzai	STT Tokyo 1	—	2025-06	32 MW (campus 70 MW)
Tama	Tama Technology Bldg (leased hyperscale)	2016-10	2020-02	17,667 m² GFA
Tama	GLP TKW1-1	2023-08	2025-02	10 MW

3. Data and methods

Table 2. Observation channels. Scene counts are after collapsing duplicate records of the same physical overpass (reprocessing builds and product versions; supplementary section S1).

Channel	Product	Resolution	Local time (JST)	Period	Independent scenes used
Daytime LST	Landsat 8/9 Collection-2 Level-2 ST (Cook et al 2014, USGS 2020)	100 m thermal on a 30 m grid	~10:30	2013-2026	261 (Inzai) + 520 (Tama)
Day/night LST	ECOSTRESS L2T LSTE (Hook and Hulley 2019, Hulley et al 2022)	70 m	all hours (ISS precession)	2018-2026	829 (Inzai) + 1,034 (Tama)
Cluster-scale LST	MODIS MOD/MYD11A2 8-day composites (Wan 2014, Wan et al 2021)	1 km	day 10:30/13:30; night 22:30/01:30	2013-2026	1,177
Land cover	Impact Observatory annual LULC (Karra et al 2021); ESA WorldCover (Zanaga et al 2022)	10 m	—	2017-2023	AOI windows
Facility energy	SHK facility-level GHG disclosures (MOE 2024)	—	—	FY2021-2023	Inzai/Shirai
Air temperature	AMeDAS station records (JMA 2026)	point, 5.5 km	monthly	2010-2026	4 stations × 198 months

3.1 LST extraction and cross-sensor logic

All satellite reads (table 2) are windowed requests over a 6 km AOI centred on the primary facility; per-pixel QA masks and a physical-validity gate (-40 to 65 °C on zone means) are applied before analysis, duplicate records of the same overpass are collapsed (keeping the latest product version), and zone means require >=40% valid pixels. Treatment footprints were verified against high-resolution imagery (supplementary figure S4). Treatment and control are differenced *within* the same scene of the same sensor, cancelling atmospheric and calibration common-mode errors — but not material-specific emissivity error: the Landsat Collection-2 emissivity derives from a static climatology (ASTER GED; Hulley et al 2015) that cannot track a 2021-2023 conversion from cropland to engineered roofing, and an unaccounted emissivity drop of 0.02-0.08 produces apparent cooling of ~1.4-5.5 K, the same sign as our daytime signal. A direct check confirms it: product emissivity over the footprint is frozen across the conversion (0.9689 vs 0.9693) — the retrieval never saw the roof. We therefore treat Landsat daytime magnitudes as upper bounds on the surface-property effect and corroborate with the ECOSTRESS estimate, whose temperature-emissivity-separation (TES) retrieval (Gillespie et al 1998) solves for emissivity per scene. Sensor-level disclosures — effective thermal resolution, deduplication keys and view-angle caveats — are given in supplementary section S1.

3.2 Treatment zones and matched controls

Treatment zones are OpenStreetMap building footprints. Our pilot used a 500-2,500 m annulus ("ring") as background; annual 10 m land cover shows the ring itself urbanised (built-up 57.6% to 61.3% over 2017-2023, ~2 pp faster than the wider background; supplementary figure S5), biasing ring-referenced differences — we retain the ring only to quantify that bias. The confirmatory reference is eight control zones fixed by design-stage rules before inspecting treatment contrasts: five industrial/warehouse roofs built before 2013 (matching the treated surface) and three stable flood-plain paddy zones (matching the pre-treatment surface). Screening for pre-period stability excluded one roof on two independent flags, leaving seven (four roofs, three paddies). This is a post-hoc quasi-experiment, not a pre-registered trial; inference therefore rests on agreement across all three reference types and on a leave-one-out sensitivity analysis over the control set — the deep-night event contrast spans -0.20 to -0.03 °C across all leave-one-out and all-controls-in variants, every one negative and non-significant (supplementary section S2). One caveat remains: the type-A roofs top operating factories and carry industrial heat of their own (~0.5 °C warmer than paddy at night), biasing the roof-referenced difference *against* detecting DC warming — one more reason no single reference is load-bearing (section 4.2).

3.3 Hypotheses and event design

We pre-specify two primary hypotheses: H1, the facility-scale deep-night (01:00-05:00 JST) pre-to-operation change at the primary facility, with its MDE bound; and H2, the cluster-scale night MDE tested against the energy-balance ceiling. All other comparisons — including the diurnal-decay signature and the Terra/Aqua split — are secondary or exploratory; because our primary inferences are non-rejections, multiple testing renders them conservative. Scene-level differences are grouped into pre (<=2020-11), construction (2020-12 to 2023-02) and operation (>=2023-03) phases; point estimates are month-of-year-demeaned (climatology from pre and operation phases) and compared with Welch tests; the design is replicated at Tama. Because each contrast is formed within a single overpass, region-wide shocks — pandemic-era economic contraction and record-breaking summers alike — are shared by treatment and control and cancel in the difference. Within the pre-period, neither matched reference shows a significant 2020 level shift ($p = 0.18$ and 0.07), whereas the development-contaminated ring does ($p = 0.017$), reinforcing matched over annular controls (supplementary section S2). Figure 2 summarises the design.

3.4 Energy-balance ceiling (primary gate)

The exclusion of large waste-heat warming rests, first, on conservation of energy — a gate immune to every surface-property confounder above. Cluster IT-load scenarios of ~100/400/650 MW span the disclosure-based lower bound, a floor-area central estimate (a per-facility accumulation across table 1; derivation in supplementary section S4.2) and a deliberate maximum (the CO2-reported bound is one-sided: the primary facility, 99,600 m² of hyperscale floor, reports only 9,364 tCO2 in FY2023 under zero-emission procurement). At PUE 1.4 — a central assumption between new-build practice (~1.3) and the industry average (1.56; Uptime Institute 2024) — the central scenario rejects ~560 MW of heat, or ~56 W m^{-2} over the ~10 km² cluster area. That area is the 3 × 3 km observation box and its immediate margin, so the gate is built at the scale it is tested; using the box's exact 9 km² raises the fluxes by ~11% and changes no conclusion (supplementary section S4.1). The resulting flux is about

6% of peak solar irradiance, comparable to a mid-density urban district (Ichinose et al 1999, Sailor 2011).

We use a steady-state advective box model, $\Delta T_{air} = F \cdot L/(\rho\, c_p\, U\, H)$ — an order-of-magnitude screening gate, not a dispersion model — with $\rho = 1.2$ kg m^{-3}, $c_p = 1005$ J kg^{-1} K^{-1}, along-wind extent $L = 3$ km (the window itself), and $(U, H) = (3$ m s^{-1}, 1000 m) for the daytime mixed layer and (2 m s^{-1}, 200 m) for the stable nocturnal layer (Stull 1988, Oke et al 2017). It caps the attainable air-temperature perturbation at ~0.05 °C (day) and ~0.35 °C (night) at cluster scale, ~0.03/0.21 °C at facility scale ($L = 1$ km, the along-wind advection path rather than the building dimension, with single-facility flux $F \approx 1.0 \times 10^2$ W m^{-2}; supplementary section S4.1). These ceilings match, to order of magnitude, independent anthropogenic-heat scaling analyses (Khanh et al 2025) and mesoscale exhaust-heat simulations (Jin et al 2020). These choices favour detection, with one exception worth stating: the full $U \times H$ sensitivity grid reaches ~1.4 °C in the sustained near-calm limit (1 m s^{-1}, 100 m), under which +2 °C would need only ~1.4 times the plausible waste heat. That cell is reported as a sensitivity limit, not a steady-state prediction: near-calm stability is a transient nocturnal state over which the steady-state model itself fails, and the ceiling is not interpreted as excluding short-lived warming episodes under such conditions. The claim under test is, however, itself a time-mean quantity, and the time-integrated constraints — the all-regime deep-night record and the cluster-scale bound — apply to it directly (full grid in supplementary section S4.1; the limit is drawn alongside the headline ceiling in figure 6b). For the surface, the ruler is the skin-temperature sensitivity $dT_s/dF = 1/\lambda \approx 0.03$-$0.09$ K per W m^{-2}; because DC heat is rejected to the air above the roof rather than conducted through insulated roofing, LST responds more weakly than air temperature, so the air-temperature ceiling bounds the LST response a fortiori.

Conversely, sustaining +2 °C in air at cluster scale would require 322 (night) to 2,412 (day) W m^{-2} — 3.2-24 GW of continuous heat, 6-43 times the clusters' plausible waste heat (a factor >1.5 even under the most adversarial combination of upper-bound load on the tight 2.3 km² built core), exceeding midday solar forcing in the daytime case; the flux needed for +2 °C in LST is larger still. Where evaporative rejection is used, part of the load leaves as latent heat and the ceiling falls further; we do not rely on this. Denominators matter when comparing studies: 56 W m^{-2} is the cluster-average flux, while over a single facility's rejection area it reaches 10^2-10^3 W m^{-2}.

The box model averages over kilometres; it says nothing about the street where a facility's neighbours live — in Inzai the nearest houses stand within ~150 m of a facility boundary, in Tama a school within ~100 m. For that near field we construct a deliberately adversarial screening envelope — an order-of-magnitude construction, not a substitute for plume-resolving dispersion modelling: full electrical load rejected as sensible heat at ground level — dry coolers at maximum during a heat wave, no evaporative fraction, and no buoyant plume rise. The envelope conserves the excess-heat flux through a wedge-shaped plume cross-section (source width 200 m, height 15 m, half-angle 10°; $\Delta T(x) = Q/(\rho\, c_p\, U\, W(x)\, H(x))$, full tables in supplementary section S4.3; the decay is plotted in figure 6a). For 36-169 MW facilities in light wind ($U = 2$ m s^{-1}) it caps the 2 m air-temperature excess at ~2-9 °C at 100 m — in any case no more than the exhaust-air excess itself (measured at 8-14 °C, Sailor et al 2026; sensitivity to a 20 °C value in supplementary section S4.3) — decaying to ~0.4-1.8 °C by 500 m and below ~0.7 °C by 1 km, where the cluster-scale box model takes over. The envelope contains the field

record: the Phoenix transects' mean +0.7-0.9 °C and peak +2.2 °C sit a factor 2-4 *below* it — the expected margin once plume rise, partial load and partial latent rejection are restored. And it quantifies the scale separation central to this Letter: warming of real, material size within hundreds of metres of a rejection array coexists, by prediction, with the absence of any kilometre-scale halo.

3.5 Minimum detectable effect

For each channel we report the smallest pre-to-operation change detectable at $\alpha = 0.05$ and power 0.8, computed on the raw within-scene differences with Welch standard errors (the difference already removes the shared seasonal cycle; MDE on demeaned series without propagating climatology degrees of freedom would understate it); a month-fixed-effects variant (supplementary section S1) changes no conclusion, and t-quantiles add <=5%. For MODIS (lag-1 $\rho \approx 0.28$ from 8-day composites and two-platform pooling) we report effective-sample-size-corrected MDEs; restricted to the single true-deep-night platform (Aqua 01:30) the MDE rises to ≈0.48 °C, above the ceiling — the cluster closure holds on the pooled record only. MDE quantifies random error; systematic reference drift is addressed by the matched-control design.

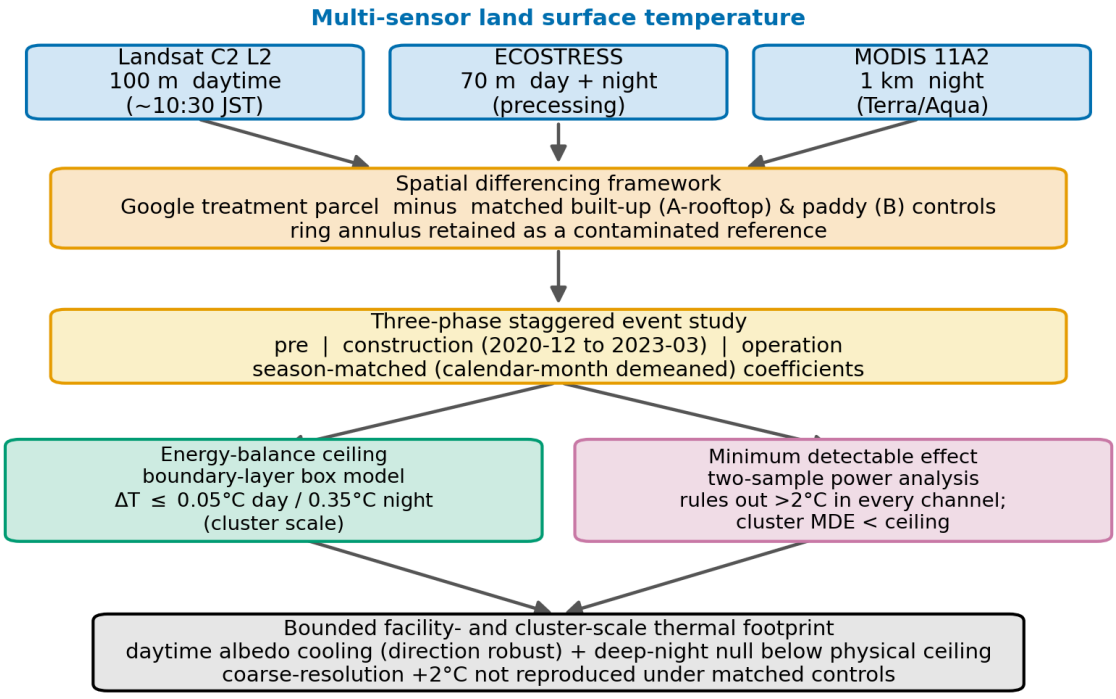


Figure 2. Design schematic: multi-sensor LST, within-scene differencing against matched controls, three-phase event study, and the energy-balance gate plus minimum-detectable-effect analysis.

4. Results

4.1 Daytime: commissioning cools the surface — significantly, under every reference

The primary facility's daytime pre-to-operation LST change is -2.22 °C against the (contaminated) ring (Welch t = -6.59), **-1.84 °C against matched pre-2013 roofs (t = -4.10) and -1.97 °C against stable**

paddy (t = -4.01) — the same sign and similar magnitude under all three references, each individually significant (figure 3). Annual 10 m land cover shows why: the parcel went from 84% cropland/16% grassland (2017) to 100% built (2023), and cooling begins already in the construction phase (section 4.4); three-epoch maps of LST anomaly, albedo and NDVI are given in supplementary figure S6. The attribution is to surfaces, not machinery: when cropland becomes an engineered roof, shortwave albedo rises (Liang 2001) and the retrieval's emissivity changes (section 3.1), while the loss of transpiring vegetation acts in the *opposite* direction (warming), making the net cooling if anything an understatement. Neither component is waste heat. And the accounting domain is narrow by design: every treatment statistic is computed over verified building-footprint pixels only, so the attribution is to the roof that replaced the crop, not to the surrounding development (controlled separately, section 3.2). The result is a robust 1.8-2.2 °C surface radiative-property cooling, opposite in sign to the claim under test. Part of the retrieved magnitude may be an emissivity artefact of the same sign (section 3.1), and any residual heat-year bias acts to *reduce* apparent cooling (supplementary section S2), so these are conservative estimates. The TES-based ECOSTRESS estimate gives -0.51 °C at 70 m and MODIS -0.36 °C (deduplicated) at 1 km — smaller as mixed pixels dilute the footprint, but one sign across three sensors. The Tama replication repeats it (-0.91 °C in operation), and the pre-2013 legacy site, where no conversion occurred, shows no comparable daytime change — as expected when the attribution is to the converted surface (supplementary section S3).

The co-developed neighbourhood strengthens the attribution. The nearest neighbouring roof, a 36,000 m² photovoltaic-covered logistics building 47 m away, is warm by day (PV albedo ~0.05-0.10), so any daytime boundary-pixel leakage biases against our signal. At night the sign of that neighbour is uncertain — rack-mounted arrays with an air gap are modelled to cool below a bare roof (Khan and Santamouris 2023) — but the deep-night estimate rests on interior pixels by construction and cannot be perturbed by leakage in either direction (supplementary section S2). All neighbours predate operation. And eroding the footprint by 20 m *deepens* the daytime cooling by a further ~0.33 °C under every reference.

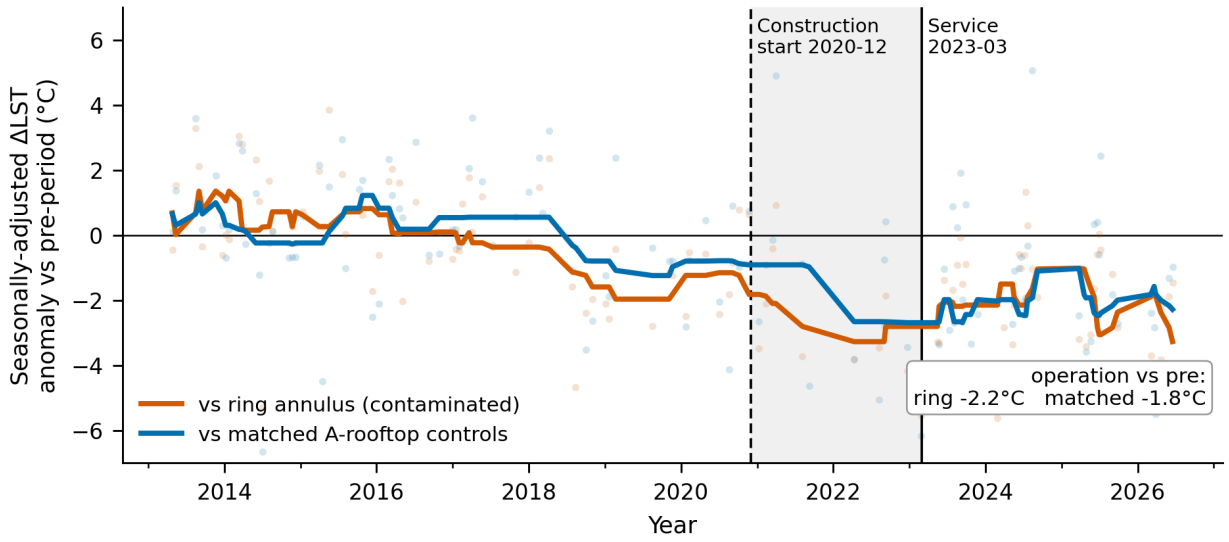


Figure 3. Daytime Landsat LST difference (treatment minus reference), month-of-year demeaned (pre- and operation-phase climatology) and normalised to each reference's pre-period mean, for the contaminated ring and the matched built-up reference. Vertical lines: construction start (2020-12, dashed) and service start (2023-03, solid). Both references show significant commissioning-phase cooling; the ring overstates it.

4.2 Night: facility-scale changes bounded near zero, with the confounding stated

At 70 m in the deep night (01:00-05:00 JST), the primary facility's pre-to-operation LST change is -0.23 °C against the ring, **-0.15 °C against matched roofs and -0.21 °C against paddy** — indistinguishable from zero in all three references (all n.s.; deduplicated n_pre = 8, n_op = 27). Interpretation requires care: at commissioning the surface changed *and* heat rejection began, components collinear in any single-site before/after, so a small warming could in principle be offset by material-driven cooling. Three observations bound what could be hidden. First, the paired levels run against the offsetting story: in operation the DC roof is slightly *warmer* than paddy at night (+0.41 °C), not colder, and roof-to-roof (materials largely differenced out) is -0.09 °C — no positive residual suggestive of masked heat. Second, the change is null against three reference types with opposite bias directions. Third, and decisively, the energy-balance gate caps any hidden facility-scale night air warming at ~0.2 °C — and the surface response a fortiori — independently of any surface-property change that might mask it in the LST record. An exploratory diurnal signature points the same way: within operation, the small positive evening anomaly (+0.33 °C, 19:00-23:00) decays to -0.26 °C by deep night (p = 0.015; figure 4) — the fingerprint of daytime storage release rather than a constant source, though this is consistency evidence, not proof.

Nor is the night result an artefact of record-heat years, although the operational window coincides with Japan's three hottest summers on record (+1.76 °C in 2023 and 2024, +2.36 °C in 2025). The deep-night difference shows no dependence on scene temperature under either reference. And the ~0.5 °C paddy-roof offset is constant across cool and hot scenes — a structural land-cover difference, not waste heat, which would warm the co-located roof reference as well (supplementary section S2). **The confirmatory statement is a bound, not a zero: facility-scale deep-night surface warming, if any, is below ~0.6 °C (ring reference) to ~1.0-1.2 °C (matched references) at power 0.8 by observation,**

and below ~0.2 °C by the energy-balance ceiling on air temperature, which bounds the surface a fortiori.

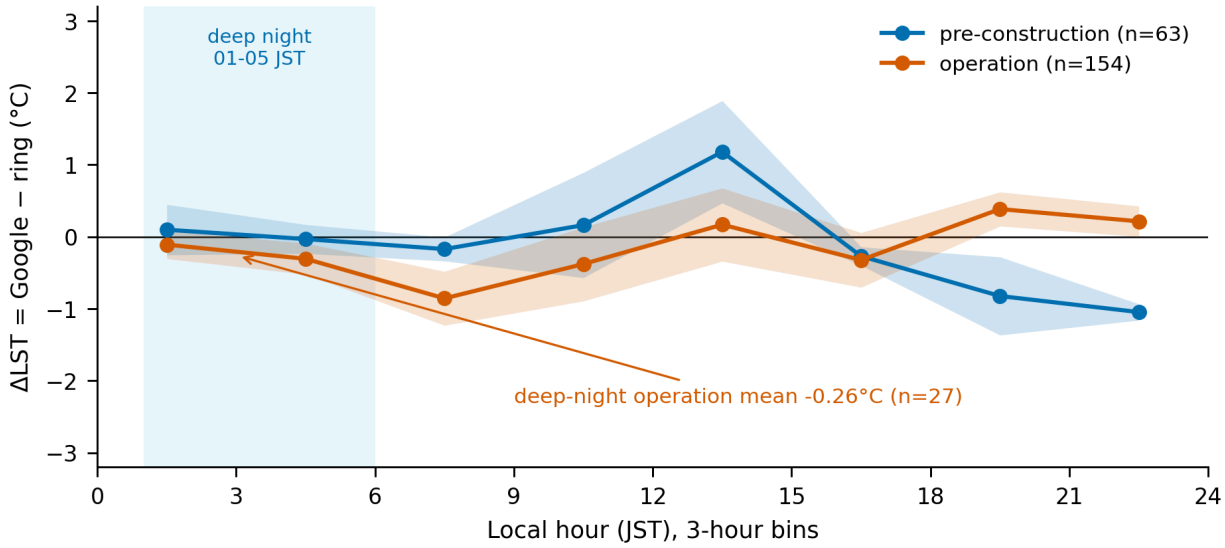


Figure 4. ECOSTRESS diurnal signature of the facility-minus-ring difference by phase (3 h local-time bins; mean ± SE; deduplicated record), with deep night (01:00-05:00 JST) highlighted. The operation-phase evening anomaly decays below zero by deep night.

4.3 Cluster scale: a bounded small positive, attributed to storage

At 1 km, MODIS night LST shows a small increase across the build-out: +0.20 °C from the pre-build-out years (<=2020) to the high-load years (>=2021) (Welch t = 2.96, deduplicated). Its temporal structure identifies it: the signal appears at the 22:30 overpass (≈+0.5 °C) and vanishes by 01:30 (≈0, n.s.) — an exploratory platform split on the post-ramp years (supplementary figure S1), but the wrong fingerprint for a constant source and the right one for evening release of daytime storage from a growing built area, consistent with the 70 m decay. This is not a null: it is a **bounded small positive (+0.20 °C), attributed to storage, sitting below the 0.35 °C waste-heat ceiling on air temperature**. The channel's value is its power: after correcting for serial dependence the MDE is 0.24-0.29 °C — below the ceiling — making this the one channel in which observation closes beneath what energy balance permits, on the pooled Terra+Aqua record (Aqua alone: Δ = +0.04 °C n.s., MDE ≈ 0.48 °C, above the ceiling). Within the pooled record, any cluster-scale night warming approaching the ceiling would have been detected. What is detected is smaller and carries a storage fingerprint.

4.4 Event study and replication

The three-phase event study (figure 5) shows, against matched roofs: daytime LST +0.68/-1.25/-1.16 °C across pre/construction/operation — cooling arrives with the surface conversion itself and persists; deep-night +0.11/+1.45/-0.03 °C — a construction-phase warm bump (disturbed bare ground) returning to zero in operation, with no post-commissioning ramp even as cluster-wide reported emissions climbed +39% (FY2022 to FY2023) and the facility's disclosed CO2 tripled: rising load without rising night temperature strengthens the null. At Tama, operation-phase deep-night differences are -0.11 °C (n = 67) and -0.11 °C (n = 62) for the two hyperscale facilities. The pre-2013 legacy DC placebo, embedded in

dense development, shows +0.48 °C (n = 63; supplementary section S3, figure S3) — the largest operational-phase night anomaly in either cluster, and still a quarter of the claimed +2 °C.

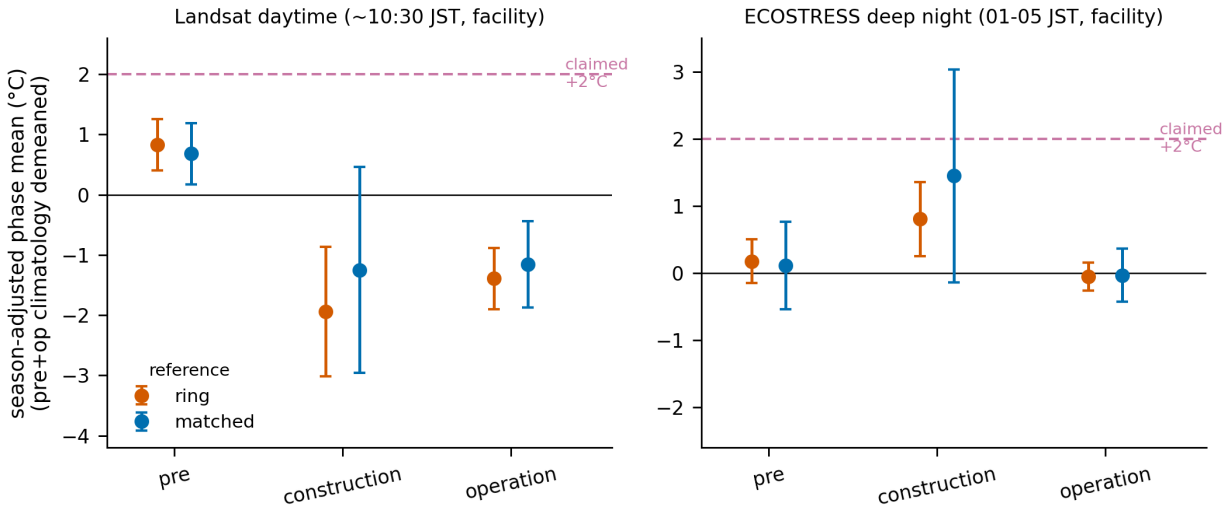


Figure 5. Three-phase season-adjusted phase means (pre/construction/operation; 95% CI; deduplicated, physically gated, month-demeaned on the pre- and operation-phase climatology) for daytime Landsat (left) and deep-night ECOSTRESS (right), under ring and matched references. The +2.07 °C coarse-resolution claim is indicated for scale.

4.5 Bounds, power and ground truth

Table 3. Core results: observed pre-to-operation changes, detection limits and physical ceilings (°C; deduplicated, physically gated, month-demeaned point estimates; RAW-series MDE at α = 0.05, power 0.8; ceilings are air-temperature box-model values — LST responds more weakly, section 3.4).

Channel (scale, window)	Observed ΔLST	MDE (LST)	Air-T ceiling	Reading
Landsat day (facility, 10:30)	-1.8 to -2.2 (significant, all references)	1.0-1.3	0.03	Surface radiative-property cooling detected; waste heat invisible by day (expected)
ECOSTRESS deep night (facility, 01-05)	-0.15 to -0.23 (n.s., all references)	0.6 (ring)/1.0-1.2 (matched)	0.21	Bounded near zero; observation excludes >=0.6-1.2 °C, physics ~0.2 °C
MODIS night (cluster)	+0.20 (evening-weighted, storage fingerprint)	0.24-0.29 (pooled; Aqua-only ≈0.48)	0.35	Bound closes beneath ceiling on pooled record; single-platform does not reach it
Tama replication (facility, deep night)	-0.11/-0.11	—	0.21	Null replicates at second site

The claimed +2 °C of LST warming exceeds the cluster-scale detection limit by a factor of ~7 and the energy-balance ceiling by a factor of 6-43 in flux terms; its exclusion rests primarily on the physics and is confirmed by every observation channel (table 3, figures 6 and 7). As an independent ground check,

the nearest meteorological station (5.5 km, prevailing summer downwind) shows no level shift relative to regional controls at the 2021 load ramp (monthly mean t = 0.14; monthly minimum t = -1.03; supplementary figure S2), consistent with, though not resolving, the sub-kilometre footprint.

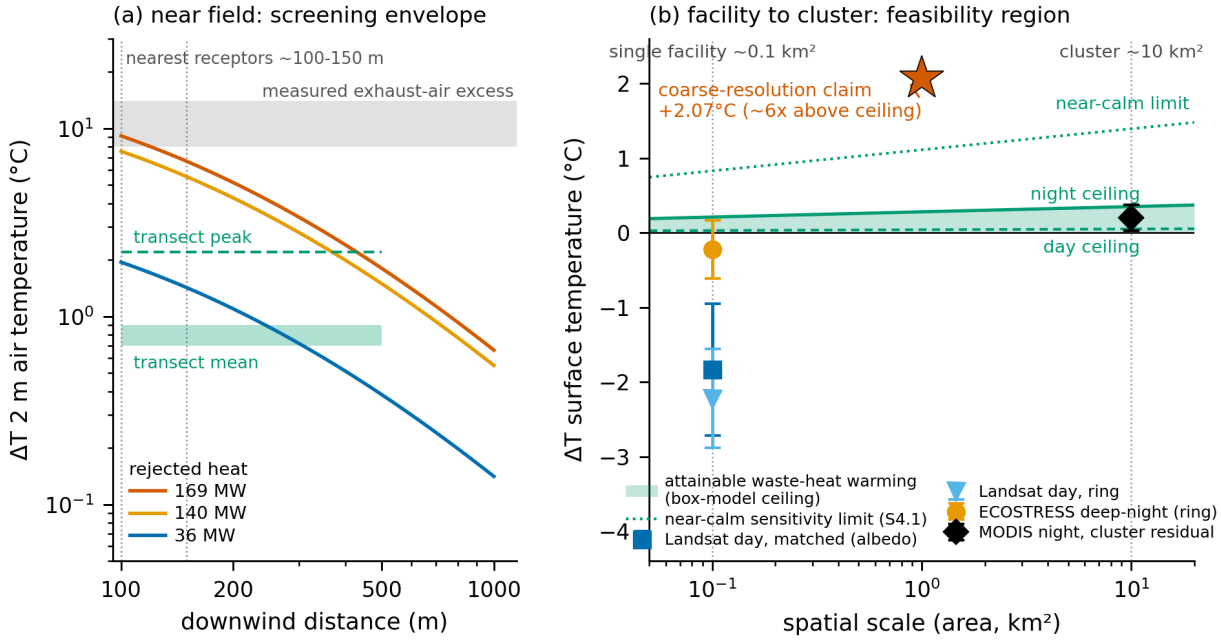


Figure 6. Scale separation between near-field and cluster-scale waste-heat warming. (a) Near field: the wedge-plume screening envelope of supplementary section S4.3 (U = 2 m s^{-1}, the three cases of that table), bounded above by the measured exhaust-air excess (grey band; Sailor et al 2026). The Phoenix transect record — downwind mean (band) and peak (dashed) — is drawn as a horizontal reference across its ≤500 m detection range rather than as a distance-resolved profile, because neither value is reported at a stated distance; the quantitative comparison with the envelope is made in supplementary section S4.3. Dotted verticals: the nearest receptors. (b) Facility to cluster: observed pre-to-operation changes versus the energy-balance feasible region by spatial scale. Shaded band: attainable waste-heat air warming (box-model ceiling; day dashed, night solid); dotted line: the sustained near-calm cell of the same U × H grid (supplementary section S4.1), reported in section 3.4 as a sensitivity limit. Points: daytime Landsat (ring and matched references, surface radiative-property component), deep-night ECOSTRESS, and cluster-scale MODIS night. The coarse-resolution +2.07 °C claim falls ~6 times above the night ceiling. The two vertical axes carry different quantities: (a) 2 m air temperature, (b) surface temperature against an air-temperature ceiling that bounds it a fortiori (section 3.4).

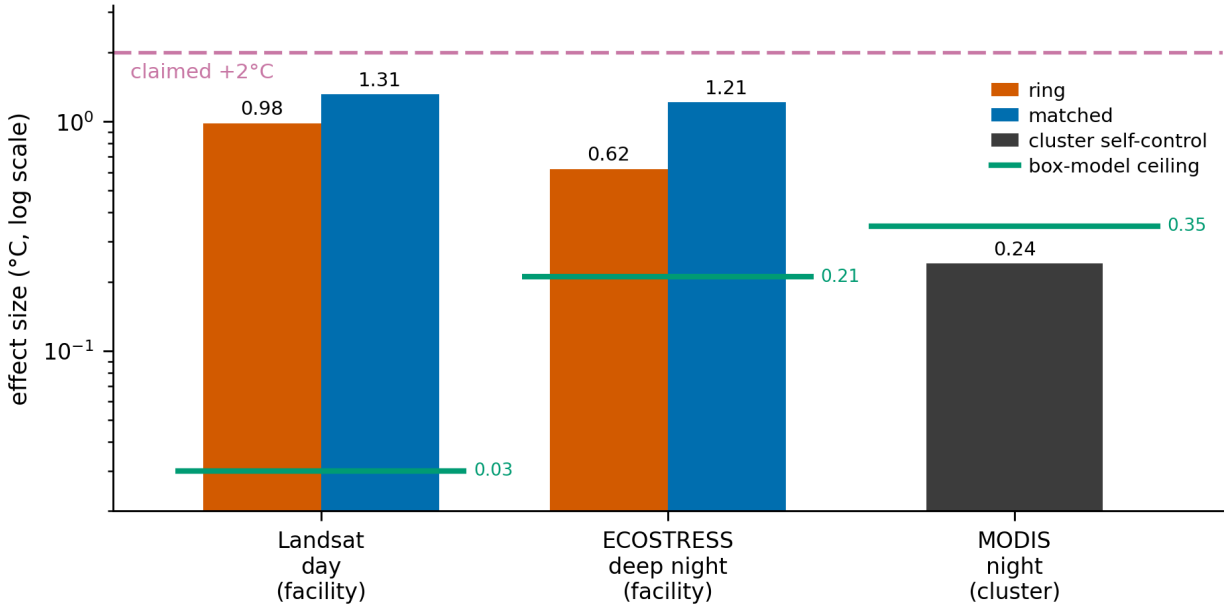


Figure 7. Minimum detectable effects by channel (ring and matched variants; deduplicated, RAW-series Welch) against the scale-matched physical ceilings (ticks) and the +2 °C claim (dashed line); log scale.

5. Discussion

The first test, and what it validates. Prospective estimates of what concentrated anthropogenic heat should do — scaling analyses (Khanh et al 2025), mesoscale simulations (Jin et al 2020), engineering plume models — have until now run ahead of any ex-post verification, a gap the Phoenix team explicitly flags. Our results are that verification: applied to the Inzai flux, those models predict tenths of a degree at night and near-nothing at kilometre scale, and across three sensors, two clusters, three reference types and thirteen years, that is what the satellite record shows. Daytime LST is set by surface radiative properties; the night observations sit at or below the modelled ceiling, with at most an evening storage-release signature. “Surface, not exhaust” summarises both.

A rapidly growing literature, and a check on it. Prospective estimates are now appearing faster than they can be reviewed: a facility-resolved simulation of California’s data centres was posted the day after this Letter was submitted (Zhang et al 2026, preprint), and a simulation of Sydney’s existing and planned facilities followed during its revision, reporting intensified night-time heatwave air temperatures (Pitman et al 2026, preprint). Neither has been peer reviewed, and we do not evaluate them here; like Marinoni et al (2026), they are prospective claims that an ex-post record of the kind assembled here can test once published. Where such an estimate can be placed on a common footing with ours the test is direct, and for the California simulation it is set out in supplementary section S4.4: the divergence from our bounds is one of where the heat is assumed to enter the energy balance (section 6). As modelled claims multiply, the protocol of section 3 supplies the ex-post check that each of them can be held to.

One framework, two published signals. Our bounds do not contradict the Phoenix transects; the energy balance predicts both. Over a facility’s own rejection area the flux reaches 10^2-10^3 W m^{-2}, so near-ground air warming of order 1 °C within hundreds of metres downwind — what the transects

measured — is expected (section 3.4); diluted over a ~10 km² cluster and read from space, the same heat cannot exceed a few tenths of a degree — what we bound. Two points on one curve, with testable predictions: transects in Inzai should find near-field air warming of at most order a degree within a few hundred metres of a rejection array, falling to tenths of a degree by ~500 m (section 3.4), and spaceborne LST around Phoenix should show no kilometre-scale waste-heat halo. We tested the second prediction directly (supplementary section S5): around a 143 MW air-cooled Phoenix-metro campus the same protocol finds a significant night LST change (+0.79 °C) — but it appears in full during construction, is indistinguishable from neighbouring non-DC development (+0.49 to +0.69 °C), and exceeds by ~6 times what waste heat could sustain at that scale. The arid night signal carries the fingerprint of desert-to-built conversion. A contemporaneous cross-sectional survey of 46 Phoenix-area data-centre buildings reports the same pairing without attributing it — surfaces ~0.5 °C warmer within 1 km, vegetation index lower (Molla 2026) — and calls the analysis exploratory; the phase decomposition supplies what a cross-section cannot. A continental-climate campus (DeKalb, Illinois) under the same protocol repeats the timing fingerprint: three quarters of its night LST change (+0.20 °C) is in place during construction, before any server load, with daytime cooling of the same sign as section 4.1 (supplementary section S5). Three climates, one decomposition: surface signals everywhere, a waste-heat halo nowhere (both cross-climate sites are shown in supplementary figure S7).

Reconciling the +2 °C claim. Our design reproduces none of it, and its magnitude sits above the mean daytime surface urban heat island of entire large cities (1.5 ± 1.2 °C; Peng et al 2012) — attributed to single buildings. Each identification gap maps onto a measured quantity: without day/night separation, albedo/emissivity and storage signals are indistinguishable from waste heat; without facility-scale resolution, mixed pixels dilute attribution (our own daytime signal shrinks from ~-1.9 °C at the 100 m Landsat scale to -0.4 °C at 1 km); without matched controls, generic peri-urban development — measured directly here (+3.7 pp built-up in our own contaminated ring) — loads onto the “DC effect”; without an energy gate, a claim requiring gigawatts per cluster passes unchallenged. Our own pipeline illustrates the stakes: an uncontrolled ring reference and duplicate records inflated our own estimates until internal audits caught both — corrections the +2 °C figure has yet to undergo. That far larger point sources leave no comparable land halo is an a fortiori check. Power stations reject several times to an order of magnitude more heat (~2 GW per large unit vs 0.56 GW for all of Inzai), yet the satellite literature on their heat is a water-plume literature (Wei et al 2023): their heat leaves through cooling water or as latent heat. That is precisely why DCs, rejecting heat directly into the inland boundary layer, are the right natural experiment.

The assessment void, and a tool to fill it. No major-market permitting regime requires assessing local temperature impact: Singapore’s green-DC standards target efficiency; Ireland and the Netherlands treat waste heat as a resource to recover; Japan’s position is described in section 2. US local instruments have in fact begun writing heat itself into data-centre zoning — a 2026 model ordinance requires that facility heat not be “perceptible at or beyond the external perimeter property line” (KRC 2026), and county-level guidance now asks developers for thermal-impact plans (CCPC 2026) — yet none of these instruments specifies how compliance would be measured. The standards are arriving before the measurement tool, and communities are left disputing a quantity nobody measures. The protocol demonstrated here — open archives, matched controls, an event design keyed to public commissioning

dates, an MDE statement, an energy budget as the outermost gate — provides the missing instrument: low-cost, replicable, ex-post verification of near-field and cluster-scale thermal impact for any facility with a known startup date. The scoped policy conclusion has three parts. At the surface, at facility-resolving scales, for the hundred-megawatt clusters studied here, the thermal footprint is bounded and small — in daytime negative. Near-source air warming of order a degree remains real where rejection density and climate favour it: the near field, not the neighbourhood kilometre, is where siting scrutiny belongs. And the gigawatt campuses now planned elsewhere scale these fluxes several-fold — the bounds reported here license no blanket clearance, only the verification protocol that any such campus can, and should, be subjected to ex post.

6. Limitations

LST is not 2 m air temperature; for air-rejected heat, skin temperature responds more weakly, so the air-temperature ceiling bounds LST a fortiori, and our results are compatible with sub-degree near-source air warming (Sailor et al 2026). That ordering is an assumption about where the heat enters the energy balance, and a contemporaneous simulation that injects it into the canopy air budget reverses it (Zhang et al 2026; supplementary section S4.4); our night bound is what discriminates between the two. The argument that LST mischaracterises heat hazard (Zhan et al 2025) does not touch its use as the claim-under-test's own yardstick. Retrieval emissivity inflates apparent daytime cooling and makes the night null conservative — a small real warming could be partially masked, though the energy budget caps the masked component at ~0.2 °C. The deep-night facility record is thin once duplicates are removed (8 pre-baseline scenes): its MDE (0.6-1.2 °C) does not close on the 0.21 °C facility ceiling, and only the cluster channel does, on the pooled two-platform record (Aqua-only ≈0.48 °C). No single reference is clean — factory roofs carry industrial heat (bias against detection), paddies a structural night offset — so inference rests on cross-reference agreement plus physics. Bounds apply to realized load during ramp-up, not nameplate: campuses reach full utilization over years. The bound is, however, anchored to the official FY2023 draw, the >=2024 windows sample the post-ramp state, and night temperatures did not rise as load climbed. View-angle variation and clear-sky sampling biases (Yang et al 2024) are registered in supplementary section S1. Two clusters in one temperate-humid climate, plus arid- and continental-climate checks at the coarsest scale only (supplementary section S5) — near-field and facility-scale observation in arid settings remains the domain of ground transects (Sailor et al 2026); per-facility event studies beyond the primary case await footprint reconstruction. Finally, the bounds are anchored to the hundred-megawatt realized loads of these clusters and do not extrapolate to the gigawatt campuses now planned elsewhere: fluxes scale linearly with load, and each such campus warrants its own ex-post test rather than clearance by analogy.

7. Conclusion

The dispute over data-centre heat has run on unvalidated models, uncontrolled observations and absent regulation. This Letter supplies the missing piece: the first ex-post, controlled satellite test of what hyperscale facilities do to the temperatures around them. The answer, for Japan's largest cluster, is threefold. Commissioning cools the daytime surface by about two degrees — significant under every

reference, a surface radiative-property signal opposite in sign to the viral +2 °C claim. Night-time surface changes are bounded within tenths of a degree of zero, closing beneath the air-temperature energy-balance ceiling at cluster scale — exactly where prospective anthropogenic-heat models put them, in their first encounter with long-term observations. And one energy budget reconciles the conflicting literature, predicting detectable near-source air warming in dry, air-cooled settings and none of the kilometre-scale surface halos claimed from coarse pixels — a prediction the arid-climate consistency check supports in a second climate. At current resolutions, what spaceborne LST sees around data centres is the surface, not the exhaust — and the protocol that shows it doubles as the ex-post assessment tool that no siting regime yet requires.

Data availability statement

Extraction and analysis code, the facility timeline, footprint-verification overlays and control-zone GeoJSON are archived at Zenodo (Jing 2026; https://doi.org/10.5281/zenodo.23083016).

The data that support the findings of this study are openly available at the following URL/DOI: https://doi.org/10.5067/ECOSTRESS/ECO_L2T_LSTE.002 (ECOSTRESS L2T LSTE); https://doi.org/10.5067/MODIS/MOD11A2.061 (MODIS 11A2); USGS Landsat Collection 2 via Microsoft Planetary Computer (https://planetarycomputer.microsoft.com); https://doi.org/10.5281/zenodo.7254221 (ESA WorldCover); www.data.jma.go.jp/obd/stats/etrn/ (JMA AMeDAS); https://eegs.env.go.jp/ghg-santeikohyo-result/search (MOE SHK disclosures).

Methods and robustness checks are given in the Supplementary Information appended to this preprint and at https://doi.org/10.1088/1748-9326/aead02/data1.

References

Chester County Planning Commission (CCPC) 2026 *Data Center Ordinance Guide* version 1.0 (https://www.chescoplanning.org/UandI/DataCenters/pdf/DataCenterOrdinanceGuide.pdf, accessed 19 August 2026)

Cook M, Schott J R, Mandel J and Raqueno N 2014 Development of an operational calibration methodology for the Landsat thermal data archive and initial testing of the atmospheric compensation component of a land surface temperature (LST) product from the archive *Remote Sens.* **6** 11244-66

Gillespie A, Rokugawa S, Matsunaga T, Cothern J S, Hook S and Kahle A B 1998 A temperature and emissivity separation algorithm for Advanced Spaceborne Thermal Emission and Reflection Radiometer (ASTER) images *IEEE Trans. Geosci. Remote Sens.* **36** 1113-26

Hook S and Hulley G 2019 ECOSTRESS tiled land surface temperature and emissivity instantaneous L2 global 70 m (ECO_L2T_LSTE) V002 [Data set] *NASA Land Processes DAAC* (https://doi.org/10.5067/ECOSTRESS/ECO_L2T_LSTE.002)

Hulley G C, Göttsche F M, Rivera G, Hook S J, Freepartner R J, Martin M A, Cawse-Nicholson K and Johnson W R 2022 Validation and quality assessment of the ECOSTRESS level-2 land surface

temperature and emissivity product *IEEE Trans. Geosci. Remote Sens.* **60** 5000523

Hulley G C, Hook S J, Abbott E, Malakar N, Islam T and Abrams M 2015 The ASTER Global Emissivity Dataset (ASTER GED): mapping Earth's emissivity at 100 meter spatial scale *Geophys. Res. Lett.* **42** 7966-76

Ichinose T, Shimodozono K and Hanaki K 1999 Impact of anthropogenic heat on urban climate in Tokyo *Atmos. Environ.* **33** 3897-909

International Energy Agency (IEA) 2024 *Electricity 2024: Analysis and Forecast to 2026* (Paris: IEA)

Japan Meteorological Agency (JMA) 2026 AMeDAS surface observation records (https://www.data.jma.go.jp/obd/stats/etrn/, accessed 6 July 2026)

Jing J 2026 Code and derived data for "Satellite observations and energy balance constrain the thermal footprint of a hyperscale data-centre cluster" [Data set] *Zenodo* (https://doi.org/10.5281/zenodo.23083016)

Jin L, Schubert S, Hefny Salim M and Schneider C 2020 Impact of air conditioning systems on the outdoor thermal environment during summer in Berlin, Germany *Int. J. Environ. Res. Public Health* **17** 4645

Karra K, Kontgis C, Statman-Weil Z, Mazzariello J C, Mathis M and Brumby S P 2021 Global land use/land cover with Sentinel-2 and deep learning *2021 IEEE Int. Geoscience and Remote Sensing Symp. (IGARSS)* pp 4704-7

Kentucky Resources Council (KRC) 2026 *Model Data Center Zoning Ordinance* version 1.4 (https://kyrc.org/wp-content/uploads/2026/01/KRC-Model-Data-Center-Zoning-Ordinance-Version-1.4.pdf, accessed 19 August 2026)

Khan A and Santamouris M 2023 On the local warming potential of urban rooftop photovoltaic solar panels in cities *Sci. Rep.* **13** 15623

Khanh D N, Varquez A C G and Kanda M 2025 Impact of anthropogenic heat on air temperature: a first-order estimate using dimensional analysis and numerical simulations *Geophys. Res. Lett.* **52** e2024GL114400

Liang S 2001 Narrowband to broadband conversions of land surface albedo I: algorithms *Remote Sens. Environ.* **76** 213-38

Marinoni A, Cambria E, Lin W, Dalla Mura M, Chanussot J, Ragusa E, Tso C Y, Zhu Y and Horton B 2026 The data heat island effect: quantifying the impact of AI data centers in a warming world (arXiv:2603.20897v3)

Masanet E, Shehabi A, Lei N, Smith S and Koomey J 2020 Recalibrating global data center energy-use estimates *Science* **367** 984-6

Masley A 2026 Data centers' heat exhaust is not raising the land temperature around where they're built (blog post, 31 March 2026; https://andymasley.com/writing/data-centers-heat-exhaust-is-not/, accessed 6 July 2026)

Ministry of the Environment, Japan (MOE) 2024 Greenhouse gas emissions calculation, reporting and disclosure (SHK) system, facility-level emissions data FY2021-FY2023 (https://eegs.env.go.jp/ghg-santeikohyo-result/search, accessed 6 July 2026)

Molla A 2026 In my backyard? Digital heat islands and the environmental justice of AI infrastructure in Phoenix *Clim. Phys. Atmos. Sci.* **3-4** 100016

Oke T R, Mills G, Christen A and Voogt J A 2017 *Urban Climates* (Cambridge: Cambridge University Press)

Peng S, Piao S, Ciais P, Friedlingstein P, Ottle C, Bréon F-M, Nan H, Zhou L and Myneni R B 2012 Surface urban heat island across 419 global big cities *Environ. Sci. Technol.* **46** 696-703

Pitman A, Fitria R, Lopez-Bravo C, Shore M, Botterill S, Sharma S, Nazarian N and Evans J 2026 Large data centres in cities risk suburban heating (Research Square, https://doi.org/10.21203/rs.3.rs-10759073/v1, preprint)

Sailor D J 2011 A review of methods for estimating anthropogenic heat and moisture emissions in the urban environment *Int. J. Climatol.* **31** 189-99

Sailor D J, Abolhassani S S and Martin E P 2026 Data center waste heat as an emerging urban thermal hazard: first field measurements of neighborhood-scale air temperature impacts *J. Eng. Sustain. Bldgs. Cities* **7** 024501

Shehabi A, Smith S J, Hubbard A et al 2025 *United States Data Center Energy Usage Report: 2025 Update* LBNL-2001758 (Berkeley, CA: Lawrence Berkeley National Laboratory) (https://doi.org/10.71468/P1RP4F)

Stull R B 1988 *An Introduction to Boundary Layer Meteorology* (Dordrecht: Kluwer)

Uptime Institute 2024 *Uptime Institute Global Data Center Survey 2024* (New York: Uptime Institute)

US Geological Survey (USGS) 2020 *Landsat 8-9 Collection 2 Level 2 Science Product Guide* LSDS-1619 (Sioux Falls, SD: USGS EROS)

Wan Z 2014 New refinements and validation of the collection-6 MODIS land-surface temperature/emissivity product *Remote Sens. Environ.* **140** 36-45

Wan Z, Hook S and Hulley G 2021 MODIS/Terra land surface temperature/emissivity 8-day L3 global 1 km SIN grid V061 [Data set] *NASA Land Processes DAAC* (https://doi.org/10.5067/MODIS/MOD11A2.061)

Wei J, Feng L, Tong Y, Xu Y and Shi K 2023 Long-term observation of global nuclear power plants thermal plumes using Landsat images and deep learning *Remote Sens. Environ.* **295** 113707

Yang Q, Xu Y, Wen D, Hu T, Chakraborty T C et al 2024 Satellite clear-sky observations overestimate surface urban heat islands in humid cities *Geophys. Res. Lett.* **51** e2023GL106995

Zanaga D et al 2022 ESA WorldCover 10 m 2021 v200 [Data set] *Zenodo* (https://doi.org/10.5281/zenodo.7254221)

Zhan W et al 2025 Satellite-derived land surface temperatures strongly mischaracterise urban heat hazard (arXiv:2509.16568, preprint)

Zhang J, Hu H, Shehabi A, He C and Sanders K 2026 Spatially concentrated heat emissions from data centers lead to localized urban warming and heat exposure (Research Square, https://doi.org/10.21203/rs.3.rs-10271868/v1, preprint)

Supplementary Information (appended for preprint)

Satellite observations and energy balance constrain the thermal footprint of a hyperscale data-centre cluster

S1. Sensor-level disclosures

Effective thermal resolution (Landsat). The Landsat 8/9 thermal band is native 100 m, distributed resampled on a 30 m grid; the primary footprint (25,197 m²) therefore contains only ~2-3 independent thermal elements, not the 27 grid cells its pixel count suggests.

Deduplication of overpass records. Both higher-resolution archives store multiple records of the same physical overpass — reprocessing builds and, for ECOSTRESS, successive product versions — which inflate raw scene counts and would double-count individual acquisitions. We collapse these before any statistic is computed. ECOSTRESS records are keyed on (orbit, scene, tile, timestamp) and reduced to one row per acquisition, retaining the v003 (reprocessed) product where a v002/v003 pair exists: this folds 268 duplicated Inzai acquisitions (1,097 to 829) and 317 at Tama (1,351 to 1,034). MODIS composites are keyed on (tile, 8-day period, platform), collapsing 24 reprocessing copies with identical values but differing production timestamps (1,201 to 1,177), while retaining Terra and Aqua as separate platforms by design (587 Terra / 590 Aqua). Landsat carries no duplicates: the 261 Inzai scenes are unique acquisition dates, and the 520 Tama records are legitimately independent observations from two overlapping WRS-2 paths (107/108), not copies. All scene counts in Table 2 and all statistics below are computed on the deduplicated records. (A same-acquisition v002/v003 reprocessing pair differs by only ~0.03-0.11 °C; once such pairs are collapsed to a single record this version step no longer enters the statistics.)

Emissivity sensitivity. LST retrieval divides observed radiance by an assumed emissivity ε. At terrestrial temperatures ($T \approx 295$ K, TIR window $n \approx 4.5$), an unaccounted emissivity error $\Delta\varepsilon$ produces an apparent LST bias of approximately $(T/n)(\Delta\varepsilon/\varepsilon)$:

Δε	apparent LST bias
0.02	~1.4 K
0.05	~3.5 K
0.08	~5.5 K

Product-emissivity check (frozen climatology). Mean Landsat Collection-2 ST_EMIS over the zones, clear scenes:

Zone	pre (2018-19)	post (2024-25)	change
Primary facility	0.9689	0.9693	+0.0004
Built-up reference roofs	0.9599	0.9602	+0.0003
Paddy reference	0.9713	0.9728	+0.0015

A real cropland-to-engineered-roof conversion should lower ε by 0.02-0.08; the product value is frozen, confirming that the retrieval never saw the roof and that daytime Landsat magnitudes over the conversion are upper bounds.

View zenith angle. ECOSTRESS points off-nadir and its view zenith angle varies between overpasses; its distribution across phases has not been audited. Thermal anisotropy over the flat roof and paddy targets is far smaller than over three-dimensional urban fabric, and within-scene differencing removes the common component, but a residual phase-correlated view-angle effect cannot be excluded; the diurnal-shape (evening-decay) comparison is therefore labelled exploratory in the main text.

Clear-sky sampling. Satellite LST samples clear scenes only, which overstates surface urban heat islands in humid climates (Yang et al 2024); this affects levels more than the within-scene differences used here.

MODIS serial dependence and MDE. On the raw (undemeaned) night-time difference series the lag-1 autocorrelation is $\rho \approx 0.29$ (pre) and 0.20 (high-load) (8-day composites, two platforms). Minimum detectable effects at $\alpha = 0.05$, power 0.8, on the deduplicated record:

Estimator	n_pre / n_high	MDE (°C)
Raw pooled	489 / 301	0.19
AR(1) effective sample size (n_eff 270 / 199)	270 / 199	0.24
Monthly aggregation	93 / 62	0.29
Aqua-only (01:30 deep night)	250 / 61	0.48

The closure beneath the 0.35 °C ceiling holds for the pooled two-platform record (0.24-0.29 °C) and fails only on the single true-deep-night platform: Aqua-only gives 0.48 °C, above the ceiling (disclosed in section 4.3).

Month-fixed-effects MDE cross-check (method B). The main-text MDEs use raw within-scene differences with Welch standard errors (section 3.5). As a cross-check that the detection statements do not hinge on that choice, we recompute them with an ordinary-least-squares month-fixed-effects model that propagates the climatology degrees of freedom correctly:

Channel	Method-B MDE (°C)	SE (coefficient)
Landsat ring, daytime	1.10	0.39
Landsat matched roofs, daytime	1.47	0.52
ECOSTRESS ring, deep night	0.85	0.30
ECOSTRESS matched roofs, deep night	1.62	0.58

Method B changes no conclusion: daytime facility MDEs remain near 1.1-1.5 °C (well below the observed 1.8-2.2 °C daytime cooling), and deep-night facility MDEs remain near 0.9-1.6 °C — the facility channel still does not close on the 0.21 °C ceiling; only the cluster channel does.

S2. Robustness to common shocks and reference choice

COVID-era level shift (pre-period internal check, daytime Landsat). Restricting the pre-period record to scenes at or before 2019 versus the eight clear scenes of 2020:

Reference	d (≤2019)	d (2020)	Welch t	p
Built-up roofs	-1.10	-2.53	-1.44	0.183
Paddy	+2.69	+1.10	-1.96	0.070
Ring (contaminated)	+1.72	+0.63	-2.70	0.017

Both matched references show no significant 2020 level shift (paddy borderline, $p = 0.07$); only the development-contaminated ring shifts significantly ($p = 0.017$), consistent with its documented urbanisation trend rather than with a pandemic effect. (Sample: ~60 clear pre-2019 scenes versus 8 in 2020, common to all three references since each is differenced within the same Landsat scene.)

Record-heat years. The operational window coincides with Japan's three hottest summers on record (nationwide anomalies +1.76 °C in 2023 and 2024 and +2.36 °C in 2025, the warmest since 1898; Japan Meteorological Agency). ENSO state over the window: El Niño winter 2023-24, neutral/weak La Niña 2024-25 and 2025-26, with a new El Niño developing from mid-2026 — the record heat is not locked to one ENSO phase.

Heat-year sensitivity of the differences. Regressions of the operation-phase difference on regional scene temperature:

Window	Reference	slope (°C per °C)	p	n
Daytime (summer)	Built-up roofs	+0.195	0.095	23
Daytime (summer)	Paddy	+0.143	0.387	23
Deep night	Built-up roofs	-0.009	0.746	27
Deep night	Paddy	-0.023	0.337	26

Daytime differences rise weakly with scene temperature (irrigated paddy stays evaporatively cool in hot conditions), so residual heat-year bias *reduces* apparent daytime cooling — conservative for that finding. Deep-night differences show no scene-temperature dependence under either reference. Deep-night yearly means of the difference against the built-up reference are non-monotonic across the record-heat years: 2023 -0.46 (n=9), 2024 +0.93 (n=4), 2025 +0.01 (n=7), 2026 -0.30 (n=7) — no rise despite escalating heat (yearly counts are small). The paddy-roof paired offset is constant across cool and hot scenes (split at the median scene temperature 16.9 °C): +0.55 °C in cool scenes (n=14), +0.50 °C in hot scenes (n=13), +0.52 °C overall (n=27), identifying it as a structural night-time land-cover difference rather than a heat-year artefact or waste heat.

Seasonal decomposition of the daytime change. The daytime estimates of section 4.1 are month-of-year demeaned across the full annual cycle (section 3.3). Applied within each half of the year, the

identical estimator places the change in the cold season:

Reference	Annual Δ	Warm season (May-Oct)	Cold season (Nov-Apr)
Matched roofs	-1.84 (t = -4.10)	-0.77 (t = -1.27, p = 0.21)	-4.09 (t = -7.25)
Paddy	-1.97 (t = -4.01)	-1.32 (t = -1.74, p = 0.089)	-3.55 (t = -6.01)
Ring (contaminated)	-2.22 (t = -6.59)	-1.37 (t = -2.94, p = 0.005)	-4.19 (t = -12.50)

The warm-season subset is not a null. Its point estimates carry the same sign as the annual ones, but on 29 pre and 29 operation scenes its minimum detectable effects are 1.8 °C against matched roofs and 2.7 °C against paddy — larger than the estimates themselves — so the subset cannot resolve an effect of the size at issue. Two consequences follow. First, supplementary figure S6 composites warm-season scenes only and therefore should not be expected to display the annual contrast; it does not, and this is not evidence against it. Second, we do not offer a mechanism-level account of the seasonal ordering: both mechanisms invoked in section 4.1 — a rise in shortwave albedo and a change in retrieval emissivity — scale with insolation and with surface temperature and would act more strongly in the warm season, not less. The strong seasonality of the reference surfaces themselves (paddy is flooded and evaporatively cool in the warm season, bare in the cold season) plausibly contributes, but we have not isolated it. The exclusion of waste-heat warming is unaffected, resting as it does on the night channels and the energy-balance gate: the daytime channel carries no waste-heat signal in either season (section 3.4). Values reproduced by `scripts/46_season_split.py`, which asserts the annual estimates against the values reported in section 4.1.

Leave-one-out over the control set (deep-night event contrast). Deduplicated, deep-night [01:00-05:00], month-demeaned point estimates (all variants n_pre = 8, n_op = 27):

Variant	Δ (°C)	t	p
All 7 surviving controls	-0.119	-0.33	0.749
Drop roof 1	-0.157	-0.41	0.686
Drop roof 2	-0.100	-0.30	0.770
Drop roof 3	-0.084	-0.23	0.824
Drop roof 4	-0.029	-0.09	0.933
Drop paddy 1	-0.202	-0.55	0.593
Drop paddy 2	-0.168	-0.45	0.662
Drop paddy 3	-0.151	-0.39	0.702
All controls incl. excluded roof (8)	-0.164	-0.47	0.648

The seven leave-one-out variants span -0.20 to -0.03 °C; every variant, including the eight-control set, is negative and non-significant. The null is insensitive to any single control.

Boundary-pixel (neighbourhood) sensitivity. The primary facility occupies one parcel of a ~50 ha master-planned park; the nearest neighbouring building is a 36,000 m² logistics roof fully covered in photovoltaics, 47 m from the treatment boundary, completed 2018 (all large neighbours

completed 2016-2020, before operation). Re-extracting the daytime Landsat difference with the treatment footprint eroded by 20 m:

Contrast (daytime)	Original	Eroded 20 m	Change
vs matched roofs	-1.84	-2.17	-0.33
vs paddy	-1.97	-2.30	-0.33
vs ring	-2.22	-2.56	-0.34

The daytime cooling deepens by ~0.33 °C under every reference when boundary pixels nearest the warm photovoltaic roof are removed — the neighbour was masking, not creating, the signal. The deep-night contrast admits no analogous test: at 70 m the operation-phase footprint resolves to only ~4 valid ECOSTRESS pixels, and a 20 m erosion leaves that pixel set unchanged (identical rows), so the deep-night estimate rests on interior pixels by construction and cannot be perturbed by boundary leakage.

Load ramp-up. Hyperscale campuses reach full utilisation gradually. The primary facility's disclosed CO_2 tripled from FY2022 (2,974 t) to FY2023 (9,364 t), and cluster-wide reported emissions rose +39% over the same interval, while the deep-night difference showed no corresponding rise — rising load without rising night temperature.

S3. Ground validation and replication detail

In-situ air temperature. Nearest station 5.5 km north of the cluster centre (prevailing summer downwind), differenced against the mean of three regional control stations (12-24 km), monthly, 2010-2026: no level shift at the 2021 load ramp in monthly means ($t = 0.14$) or monthly-mean minima ($t = -1.03$). A 5.5 km point station cannot resolve a sub-kilometre footprint; this is a consistency check, not an attribution test.

Tama replication. Second cluster, western Tokyo. Primary replication case (17,667 m² leased hyperscale building, in service 2020-02): operation-phase daytime difference -0.91 °C ($n = 191$); summer-only pre-to-operation change +0.18 °C (n.s. — the site was already low-LST before conversion). Deduplicated deep-night operation-phase differences: -0.11 °C ($n = 67$) for the replication case and -0.11 °C ($n = 62$) for the second hyperscale facility; the pre-2013 legacy DC placebo shows +0.48 °C ($n = 63$).

S4. Energy-balance parameters, derivations and sensitivity

S4.1 Box-model parameters. $\Delta T_{air} = F \cdot L/(\rho\, c_p\, U\, H)$ with $\rho = 1.2$ kg m^{-3} and $c_p = 1005$ J kg^{-1} K^{-1} (dry air); $L = 3{,}000$ m at cluster scale (the along-wind extent of the 3 × 3 km observation window) and 1,000 m at facility scale. Boundary-layer scenarios follow textbook typical values for the daytime convective mixed layer and the stable nocturnal layer (Stull 1988, Oke et al 2017):

Full U × H grid, ΔT (°C) at the cluster flux $F = 56$ W m^{-2} (headline scenarios in bold: daytime mixed layer U3/H1000; stable nocturnal layer U2/H200; the sustained near-calm cell U1/H100 is transient, see below):

ΔT (°C)	H = 100 m	H = 200 m	H = 1,000 m
U = 1 m s^{-1}	1.39	0.70	0.14
U = 2 m s^{-1}	0.70	**0.35**	0.07
U = 3 m s^{-1}	0.46	0.23	**0.05**

At facility scale the same model uses L = 1 km and the single-facility flux F ≈ 1.0 × 10^2 W m^{-2} (a ~100 MW facility over ~1 km^2; section S4.2), giving the 0.03 °C (day) and 0.21 °C (night) ceilings quoted in the main text.

Area convention. The flux arithmetic rounds the 3 × 3 km observation box to ~10 km^2; using the box's exact 9 km^2 gives 62 W m^{-2} and raises every ceiling by ~11% (night 0.35 → 0.39 °C), changing no conclusion — the pooled MODIS MDE (0.24-0.29 °C) still closes beneath the ceiling, and the flux required for the claimed +2 °C remains several times the plausible waste heat.

The grid spans 0.05-1.4 °C. The near-calm cell is reported in the main text rather than suppressed, as a sensitivity limit rather than a steady-state prediction: near-calm stability is a transient nocturnal state over which the steady-state assumption itself fails, and the ceiling is not interpreted as excluding short-lived warming episodes under such conditions. The claim under test is itself a time-mean quantity, to which the time-integrated constraints (the all-regime deep-night record and the cluster-scale bound) apply directly.

S4.2 Cluster load scenarios and the 560 MW figure. The central scenario accumulates per-facility loads across table 1 of the main text: disclosed IT capacities where public (Colt DC1 8, DC3 27, DC4 ~5 initial; Equinix TY12x 30-54, TY13x 8-20; AirTrunk TOK1 60-100 initial; STT Tokyo 1 32 MW) plus floor-area-scaled estimates for the two undisclosed facilities (the primary case, 99,600 m^2 GFA, ~40-60 MW by analogy with same-class campuses; DPDC, 31,400 m^2, ~18 MW). Accumulation gives ~250 (conservative) / 400 (central) / 600-650 (maximum) MW of IT load; at PUE 1.4 the central scenario rejects 400 × 1.4 = 560 MW. An independent lower bound comes from mandatory GHG disclosures: reversing reported emissions through the utility emission factor gives ~87-126 MW of cluster draw (FY2021-FY2023) — one-sided, because zero-emission procurement suppresses reported CO2 without reducing physical load. The central estimate is therefore deliberately generous to the warming hypothesis: giving the cluster the maximum plausible heat and still finding a null is the conservative direction for a bounding exercise.

S4.3 Near-field adversarial screening envelope (wedge construction). For the near field the excess-heat flux is conserved through a wedge-shaped plume cross-section: $\Delta T(x) = Q_{sens}/(\rho\, c_p\, U\, W(x)\, H(x))$, $W(x) = W_o + 2x \tan\theta$, $H(x) = H_o + x \tan\theta$, with source width W_o = 200 m (a rooftop cooling array), source height H_o = 15 m, and neutral-stability half-angle $\theta = 10°$. Worst-case assumptions, each of which inflates the envelope (an order-of-magnitude screening construction, not a substitute for plume-resolving dispersion modelling): nameplate load at heat-wave maximum (typical utilisation is 30-50%); all heat sensible (dry coolers, no evaporative fraction); no buoyant plume rise (the exhaust excess of ~8-14 °C guarantees rise in reality); light wind U = 2 m s^{-1}. Processes omitted from the wedge — building downwash, crosswind meander, stability-class variability — each dilute the plume further, so their omission keeps the construction an upper bound.

Q_sens	100 m	250 m	500 m	1,000 m
36 MW (smallest transect facility)	1.9	0.9	0.4	0.1
140 MW (100 MW IT × PUE 1.4)	7.6	3.4	1.5	0.5
169 MW (largest transect facility)	9.1*	4.1	1.8	0.7

Values in °C at U = 2 m s^{-1} (multiply by 2/3 for U = 3 m s^{-1}); the asterisked value reaches into the measured exhaust-air excess range (8-14 °C; Sailor et al 2026), which caps any downwind 2 m warming regardless of the dilution model; no value exceeds its upper end. A stable-stratification variant (θ = 5°) raises the mid-field values by ~50-100% but is physically inconsistent with the full-load heat-wave scenario it would have to accompany. Anchoring the exhaust cap instead at the ~15-20 °C engineering value raised in review changes nothing in the table: no wedge value exceeds 9.1 °C, so a 20 °C cap never binds and every mid- and far-field entry is unchanged. The field record sits a factor 2-4 below the corresponding worst case (transect mean +0.7-0.9 °C, peak +2.2 °C), the expected margin once plume rise, partial load and partial latent rejection are restored.

S4.4 Comparison with a prospective facility-resolved simulation. A physics-based urban-climate simulation of California's data centres (Zhang et al 2026, preprint), posted one day after this manuscript was submitted, couples a facility-level inventory to WRF with a single-layer urban canopy scheme on a 4 km grid. It is the most directly comparable prospective estimate available, and section 5 of the main text draws on the comparison set out here. Its reported sensitivities — obtained by linear fits across grid cells — are 0.012 °C per W m^{-2} for 2 m air temperature and 0.048 °C per W m^{-2} for land surface skin temperature. We reproduce its two published operating points from those slopes as a check that we read its flux convention correctly (facility capacity divided by the 16 km^2 cell): 1 GW in the Santa Clara hotspot cell gives 62.5 W m^{-2} and predicted changes of 0.75/3.00 °C against its reported 0.80/3.11 °C; 100 MW in one cell gives 6.25 W m^{-2} and 0.075/0.30 °C against its reported 0.08/0.3 °C.

Applying those slopes at the Inzai cluster flux (56 W m^{-2}, section S4.2):

Quantity	Simulation	This study	Ratio
dT_s/dF	0.048 K per W m^{-2}	0.03-0.09 (section 3.4 ruler)	inside our range
ΔT_{air} at 56 W m^{-2}	0.67 °C	0.35 °C (nocturnal ceiling; 1.4 °C near-calm cell)	1.9×
ΔT_s at 56 W m^{-2}	2.69 °C	0.24-0.29 °C (measured cluster night MDE)	9.3×
$\Delta T_s/\Delta T_{air}$	3.9	< 1 (heat rejected above the roof)	opposite ordering

Three features of the comparison bear on our conclusions. First, the agreement is closer than the headline numbers suggest. The simulation's skin-temperature sensitivity falls inside the range we adopt independently, and its state-wide mean skin response — below 0.1 °C — lies beneath our detection bound of 0.24-0.29 °C, so the waste-heat contribution it predicts for a typical cell would be invisible in our record, while the +0.20 °C we do measure is attributed to storage (section 4.3 of the main text). At the level of air temperature the two treatments differ by a factor of order unity rather than by the factor of nine seen at the surface: its air-temperature prediction at our flux, 0.67

°C, exceeds our nocturnal ceiling by a factor of 1.9 and remains below the near-calm cell of the same U × H grid (1.4 °C, section S4.2). The 3.11 °C figure is the single strongest cell in the state, where approximately 1 GW is concentrated within 16 km². Second, the one substantive divergence is the ratio of skin to air response. That simulation incorporates anthropogenic heat into the canopy air energy budget, from which the surface warms; its authors note that the single-layer scheme "does not explicitly resolve vertical variations in intra-canopy heat exchange, turbulence, or radiative processes" and may therefore bias the representation of anthropogenic heat effects. Heat leaving a rooftop rejection array 8-14 °C above ambient, with the associated momentum and buoyancy, does not pass through the surface energy balance in that way, which is why we treat the air-temperature ceiling as bounding the LST response a fortiori (section 6 of the main text). If the simulated ordering held at our flux, the Inzai night surface would show approximately 1.35 °C; the measured bound of 0.24-0.29 °C excludes it. Third, that study attributes the ~2 °C satellite claim to land-cover modification, vegetation loss, albedo change, altered storage and roughness rather than to operational waste heat, its own simulations holding land surface characteristics constant — the decomposition this paper reaches observationally.

Four differences in convention prevent a direct comparison of absolute temperature changes, which is why the comparison above rests on the dimensionally normalised slopes rather than on reported maxima. (i) Its Scope 1 heat emission is nameplate capacity times a load factor of unity, which its authors describe as an upper-bound scenario; our 56 W m⁻² is a central load estimate. (ii) Its grid cell is 16 km² with a 4 km along-wind extent, against our ~10 km² window and 3 km extent. (iii) It includes Scope 2 heat released at generating plants (41% of the state total, though only 3% in the Santa Clara cluster); our budget counts facility rejection only. (iv) Its main simulations release all heat as sensible; in its 30%-sensible experiment the Santa Clara maxima fall from 3.11 to 2.24 °C and from 0.80 to 0.62 °C, the same direction as the latent-partitioning allowance we decline to claim (section 3.4). A further structural difference matters for the cross-climate checks: construction-phase heat is excluded from that inventory by design, so the simulation cannot generate the pre-operational night signals we observe at Goodyear and DeKalb (section S5) — independent support for reading those signals as conversion rather than exhaust. The arithmetic of this section is reproduced by `scripts/44_zhang2026_crosswalk.py` in the archived code.

S5. Cross-climate checks: an arid and a continental cluster

Design. The framework of section 5 predicts that spaceborne LST should show no kilometre-scale waste-heat halo even where near-source air warming has been measured on the ground. We test this in the one metro area with published ground-truth transects (Sailor et al 2026). Because the transect facilities are anonymised, we selected the largest campus in the same corridor with public dates: a 147-acre, 143 MW (Phases I-II) air-cooled campus of Microsoft's zero-water design in Goodyear, AZ (land acquired 2019-04, on-site construction from 2020, first phase in service 2023-04); we treat its rejection as all-sensible, the worst case of section S4.3. Phases are anchored to the public dates (acquisition and first-phase service), so the construction phase includes roughly a year of pre-disturbance, which dilutes rather than inflates its estimate. The main-analysis protocol is applied unchanged: MODIS MOD/MYD11A2 night and day composites 2013-2026 (1,203 scenes,

deduplicated to 1,180), a 3 × 3 km treatment window, three irrigated-farmland control boxes at 12-22 km (satellite-verified stable), phases cut at 2019-04 and 2023-04, month-of-year demeaning, Welch tests.

Result. The night-time pre-to-operation change is +0.79 °C (t = 3.4), robust against each control individually (+0.63 to +1.03 °C). The daytime change is indistinguishable from zero (+0.12 °C, n.s.). Figure S7 shows both cross-climate sites together.

Attribution. Three facts identify the night signal as land conversion rather than waste heat. First, timing: the construction-phase change (+0.86 °C, t = 3.8, on the same month-demeaned convention) equals the operational one — the signal is complete before the first server switches on. Second, energy balance: the campus's 143 MW IT load at PUE 1.3 rejects ~186 MW, or ~21 W m^{-2} over the 9 km^2 window, capping attainable night warming at ~0.13 °C under the standard nocturnal scenario — a factor ~6 below the observed change; in the sustained near-calm cell of the same U × H grid (section S4.1) the ceiling rises to ~0.5 °C, which still lies beneath the observed +0.79 °C. Third, development controls: two equally-sized boxes over contemporaneous non-DC development in the same corridor — a residential subdivision and a warehouse district — show night changes of +0.69 °C (t = 17.2) and +0.49 °C (t = 4.7) against the same farmland controls; the DC box's excess over them (+0.11 °C, t = 0.45, and +0.30 °C, t = 1.17) is not significant, though this comparison has power only to exclude differences larger than ~0.4 °C. A land-cover audit adds a monotone dose-response (figure S7c): built-up fraction rises +37 points in the treatment box against +24 and +14 in the development boxes and ≤1.5 points in two farmland controls (the third farmland box itself urbanised by +10 points, biasing the farmland reference warm — against the detected excess). The warehouse district's daytime change is −0.80 °C (t = −4.3): the same bright-roof cooling detected at Inzai, in the opposite climate. A contemporaneous study of the same metropolitan area reaches the descriptive part of this result from a different design and stops short of attribution: an exploratory cross-section of 46 Phoenix-area data-centre buildings reports mean LST of 39.74 °C within 1 km against 39.26 °C city-wide, together with a lower vegetation index (0.15 against 0.17), and states that it does not establish causality (Molla 2026). The pairing of a warmer surface with less vegetation is what a conversion signal looks like; separating it from waste heat requires the phase structure, energy gate and development controls applied here, which a cross-section against a city-wide mean cannot supply. Its environmental-justice dimension — proximity of facilities to lower-income and minority populations — is outside the scope of this paper and is not addressed by our design. (A 1 km campus-only box retains too few QC-valid scenes to analyse — n = 6 pre / 1 operation — and is reported as unusable. The channel's night MDE, ~1.0 °C, does not close beneath the 0.13 °C ceiling: the check constrains attribution, not magnitude.)

Continental check. The same protocol was run on a humid-continental hyperscale campus: Meta's DeKalb, Illinois data centre, on the southern edge of a small university city surrounded by cropland, 100 km west of Chicago. Public dates: ground broken 2020-06; the first phase (~0.9 million sq ft) online 2023-11; full build-out (~2.3 million sq ft) reached 2024-12 — the operational window spans a load ramp, so we report the full window (>=2023-11) and the post-build-out window (>=2025) side by side. The 3 × 3 km treatment box is a mixed development — the campus, an adjacent logistics estate built over the same period, the I-88 tollway across its northern edge, and cropland

over roughly its southern half — quantified by the land-cover audit (2017-2023, the product's span): built-up fraction 2.8% → 21.8%, against +4.1 and +2.8 points in two development-comparison boxes (a logistics/farmland box near Rochelle, 25 km southwest, and the DeKalb-Sycamore commercial fringe, 7.5 km north) and ≤0.3 points in three satellite-verified farmland controls.

With the pre-period extended to 2003 (n = 1,143 night scenes), the night-time change is +0.20 °C over the full window (t = 2.5, p = 0.016) and +0.15 °C (not significant; MDE 0.37 °C) after full build-out. **Attribution rests on timing** (figure S7b): three quarters of the night change is already in place during construction (+0.16 °C, p = 0.018), before the first server switched on, while neither development-comparison box moves in the construction phase — waste heat cannot produce a signal that precedes operation. The energy gate is consistent but, unlike the arid case, not decisive on its own: a floor-area-scaled ~110 MW IT load at PUE 1.0-1.2 (the operator reports a fleet-wide PUE near 1.1) gives 12-15 W m^{-2} and a 0.08-0.09 °C night ceiling under the standard nocturnal scenario — a factor 2.2-2.7 below the full-window change — but the ceiling reaches 0.30 °C in the sustained near-calm cell of the U × H grid (section S4.1), where it no longer excludes the observation; and because the load is an estimate, we state the break-even points: waste heat alone could reproduce the full-window change only at ~270-300 MW IT (above published figures for the site), though the post-build-out change at ~200-225 MW (within their range). The development boxes serve a narrower purpose than in the arid case: their night changes over the same period (+0.19 and +0.32 °C — the latter with essentially no land conversion) show that non-farmland boxes in this landscape shift by comparable amounts, though the comparison has power only to exclude treatment-development differences larger than ~0.4 °C. The daytime change is -0.47 °C (p = 0.008) — the same sign as the primary cluster's bright-roof cooling, but not larger than the development boxes (-0.23, n.s., and -0.53, p = 0.004) and against a farmland-control baseline noise of ~0.2 °C: we read it as directionally consistent, not as an independent replication. The night MDE (0.24 °C full window) does not close beneath the waste-heat ceiling; this check constrains sign and timing, not magnitude.

Reading. In the humid-subtropical cluster, conversion cools the daytime surface and leaves the night unchanged; in the arid corridor, conversion warms the night surface and leaves the day unchanged; in the continental cluster, a night increase is largely in place during construction — before any server load — alongside daytime cooling of the same sign as the primary cluster. All three are surface radiative/storage signals; in no case does the timing admit a waste-heat reading, and in none is a waste-heat term required. An uncontrolled before/after would have booked +0.79 °C to the data centre — the failure mode of section 5 of the main text, demonstrated in situ.

S6. Supplementary figures

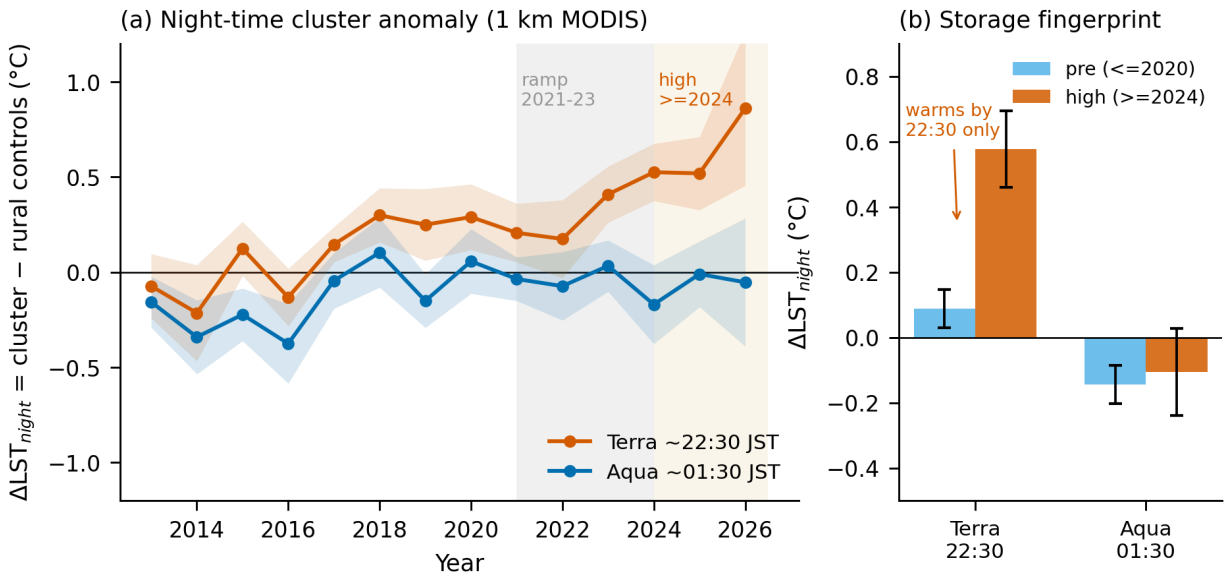


Figure S1. Cluster-scale MODIS night-time difference (treatment box minus control boxes), by platform: Terra (~22:30 JST) and Aqua (~01:30 JST). The build-out signal appears at 22:30 and vanishes by 01:30 — the storage fingerprint. Panel (b) and the platform split use the conservative post-ramp subset (high >=2024, ramp 2021-23 excluded); the pooled headline contrast in the main text uses >=2021.

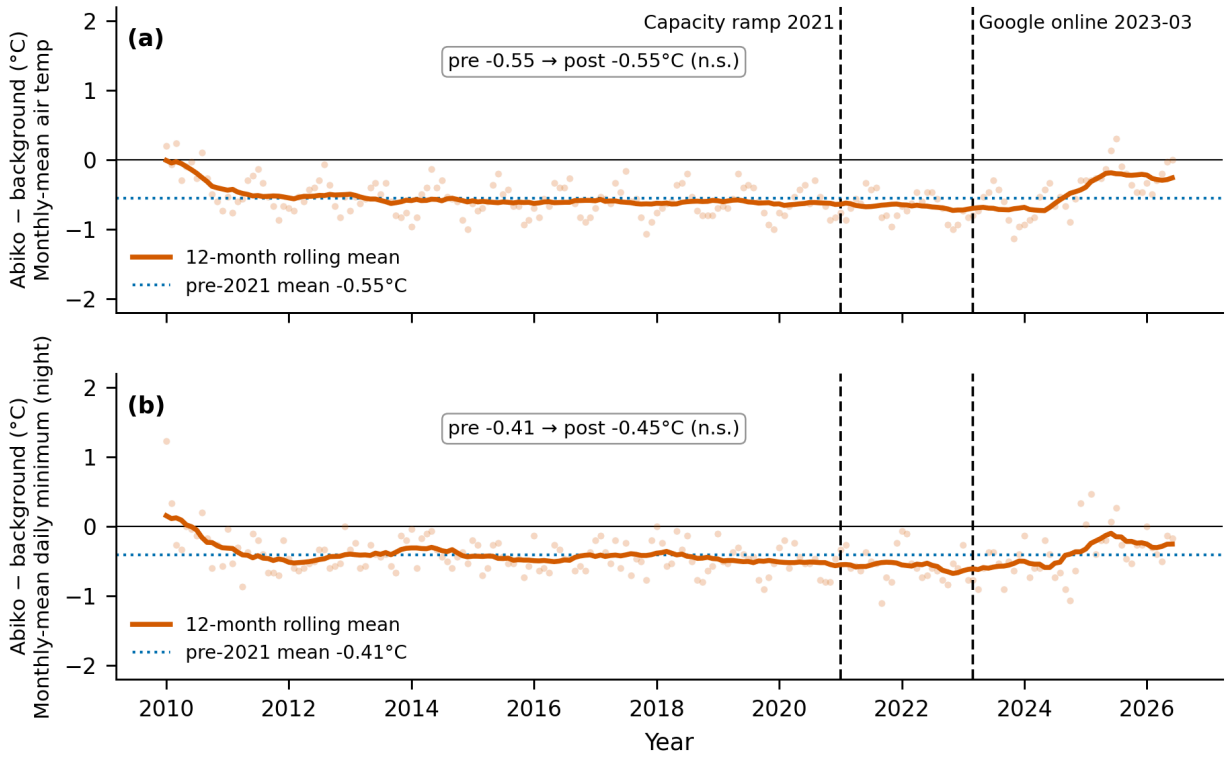


Figure S2. In-situ air-temperature check: nearest station (5.5 km) minus regional control mean, monthly means and monthly minima, with the 2021 cluster load ramp marked.

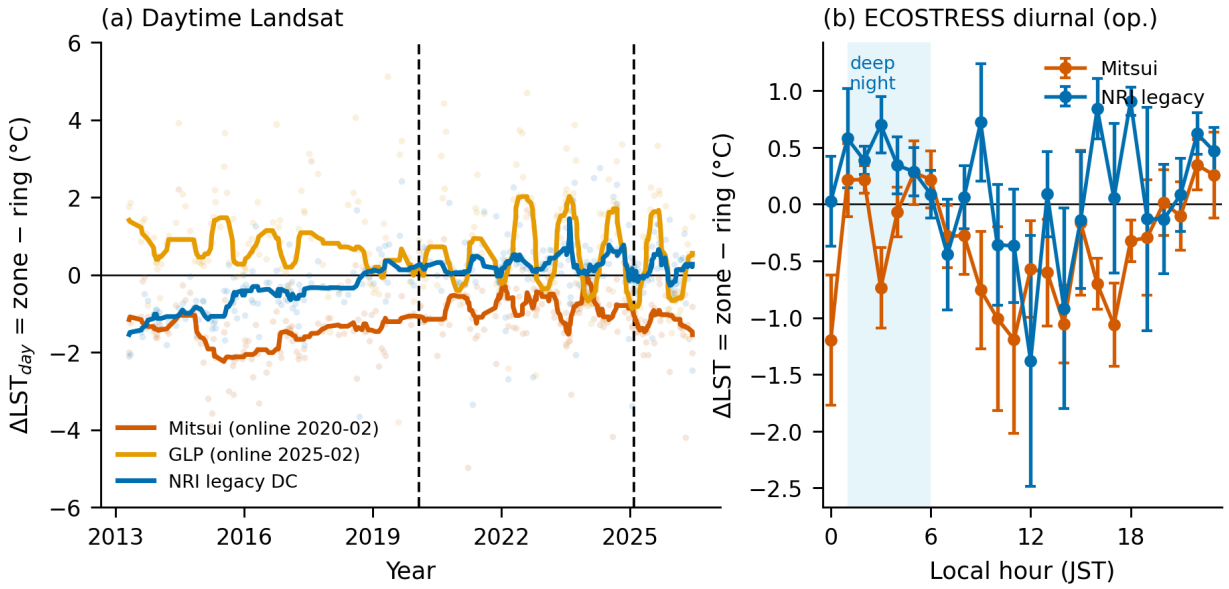


Figure S3. Tama replication: daytime three-zone differences and operation-phase ECOSTRESS diurnal profile for the replication case and the legacy-DC placebo.

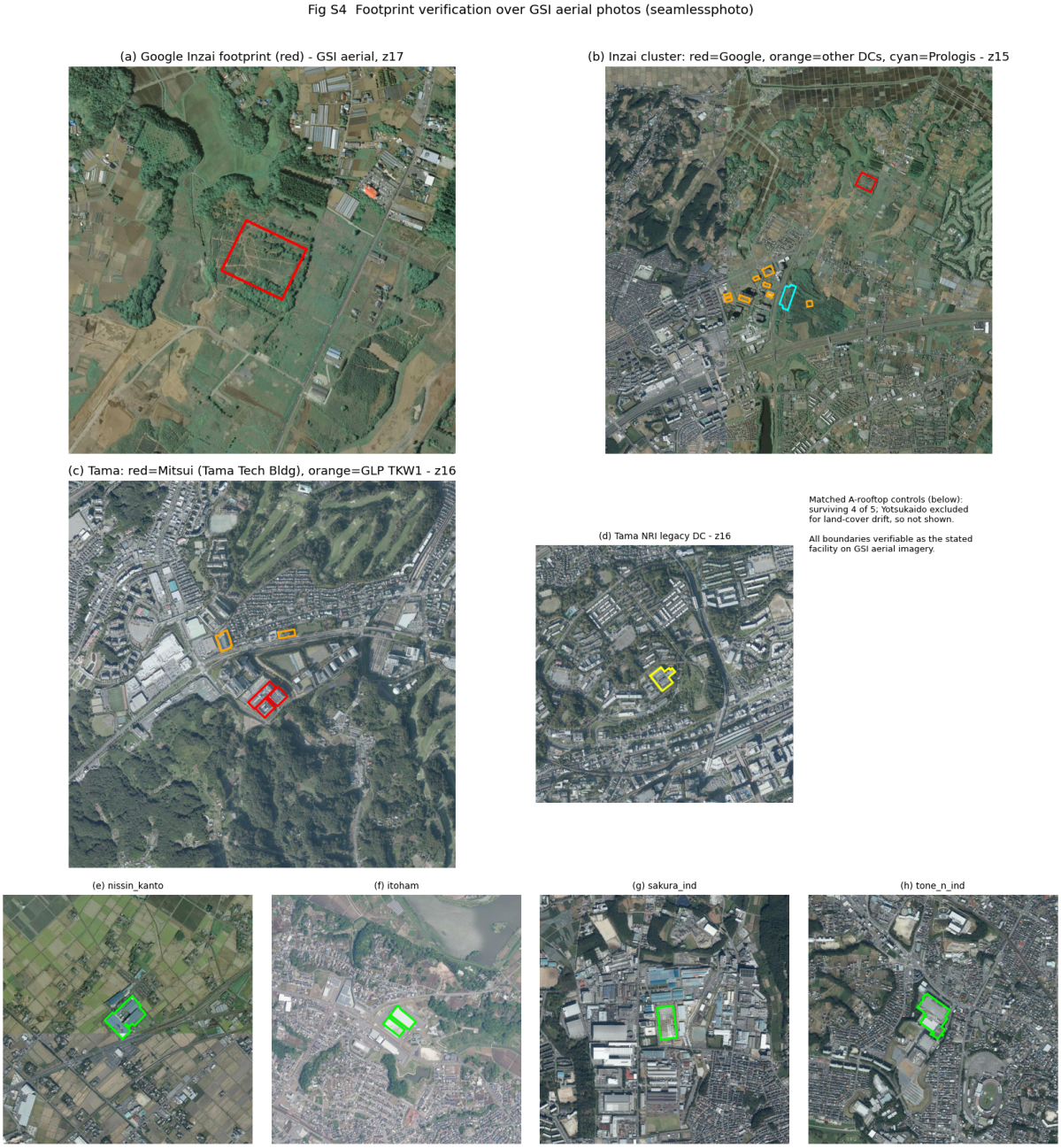


Figure S4. Footprint verification: all analysis polygons overlaid on aerial photography (treatment, cluster, replication zones, and the four surviving built-up reference roofs).

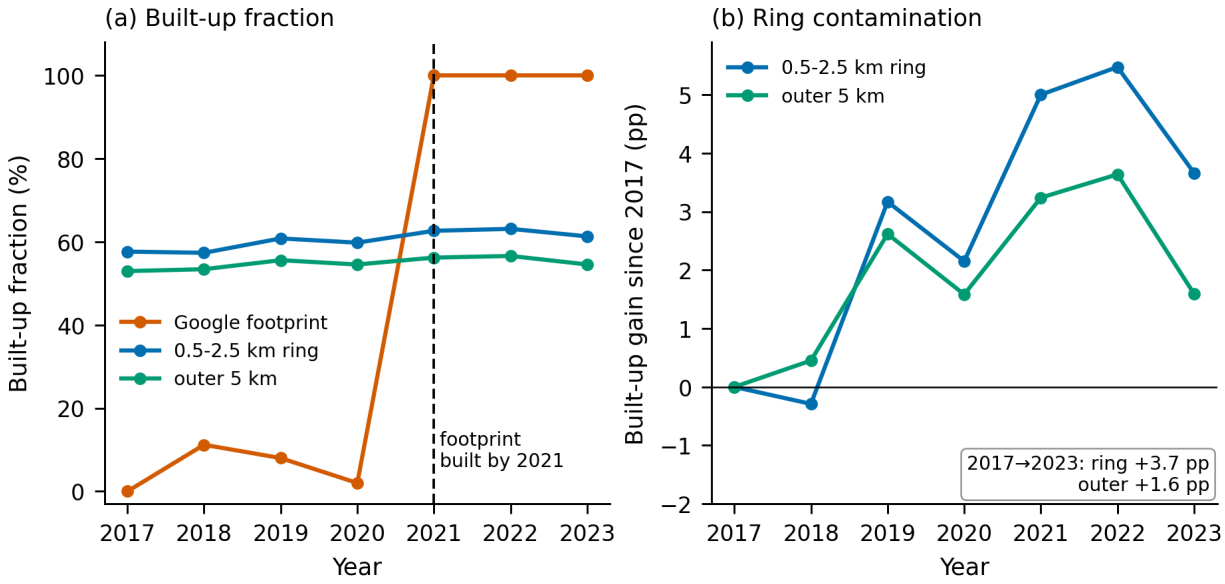


Figure S5. Land-cover trajectories (10 m annual product): built-up fraction of the treatment parcel, the ring, and the 5 km background, 2017-2023 — the ring urbanises ~2 pp faster than the background, quantifying its contamination.

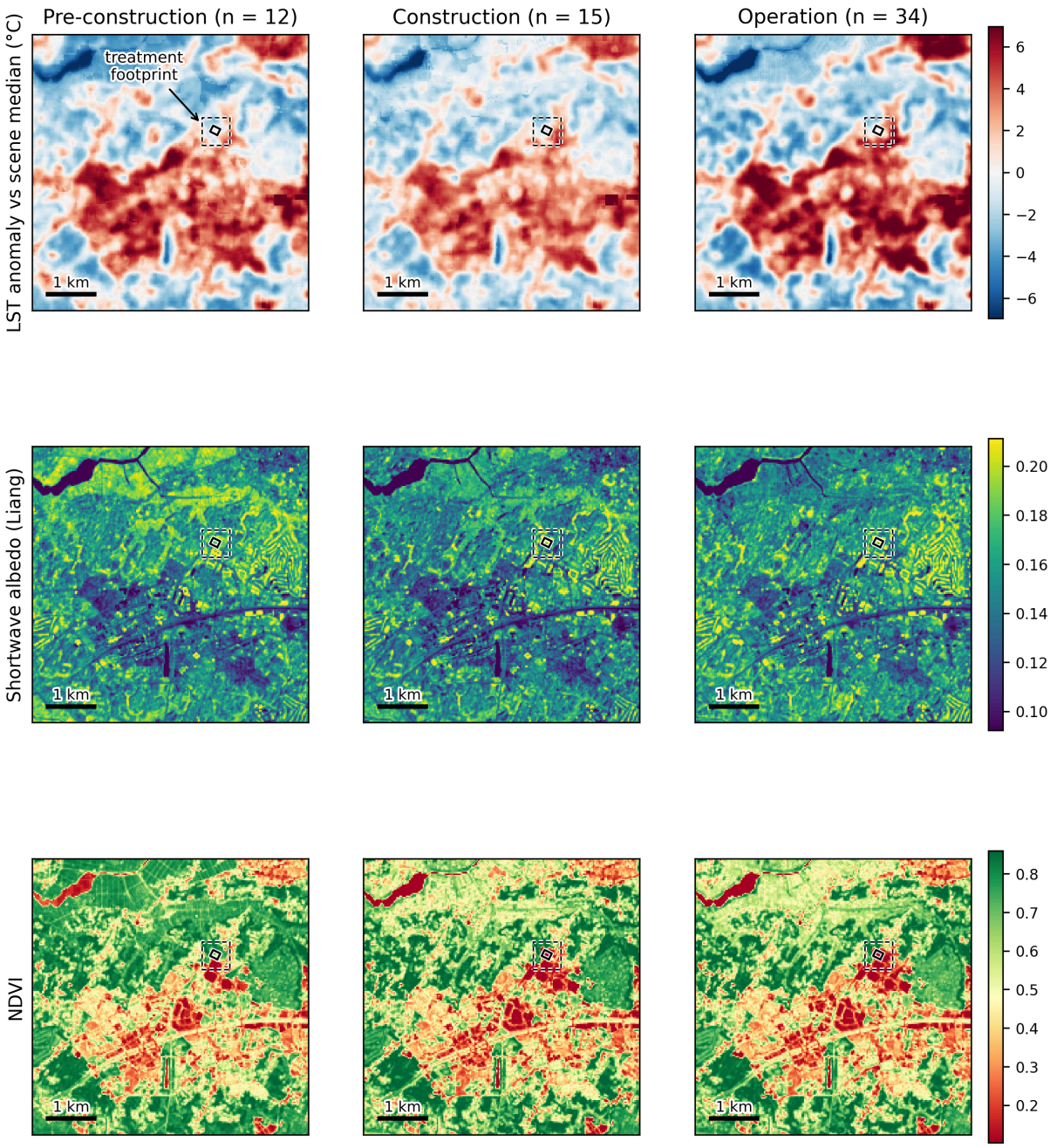


Figure S6. Three-epoch composites over the primary-facility window (3 km radius): LST anomaly relative to each scene's window median (top; the anomaly basis removes the differing weather and month mix of the epochs), Liang shortwave albedo (Liang 2001; middle) and NDVI (bottom), for pre-construction, construction and operation warm-season (May-October) scenes. The treatment footprint is outlined in black inside the dashed locator box; it spans ~160 m, about 3% of the window width. Its conversion is visible in all three variables: between the pre-construction and operation epochs the footprint mean rises from 0.18 to 0.20 in shortwave albedo, falls from 0.59 to 0.10 in NDVI, and rises from +0.09 to +0.72 °C in LST anomaly. The last of these is on a different convention from section 4.1 of the main text and is not comparable with it: these are warm-season composites referenced to the median of the surrounding

window, whereas the main-text estimate is an all-season, month-of-year-demeaned difference against matched pre-2013 roofs and stable paddy. The seasonal decomposition of that estimate is given in supplementary section S2; the warm-season subset used here cannot resolve an effect of the size reported annually.

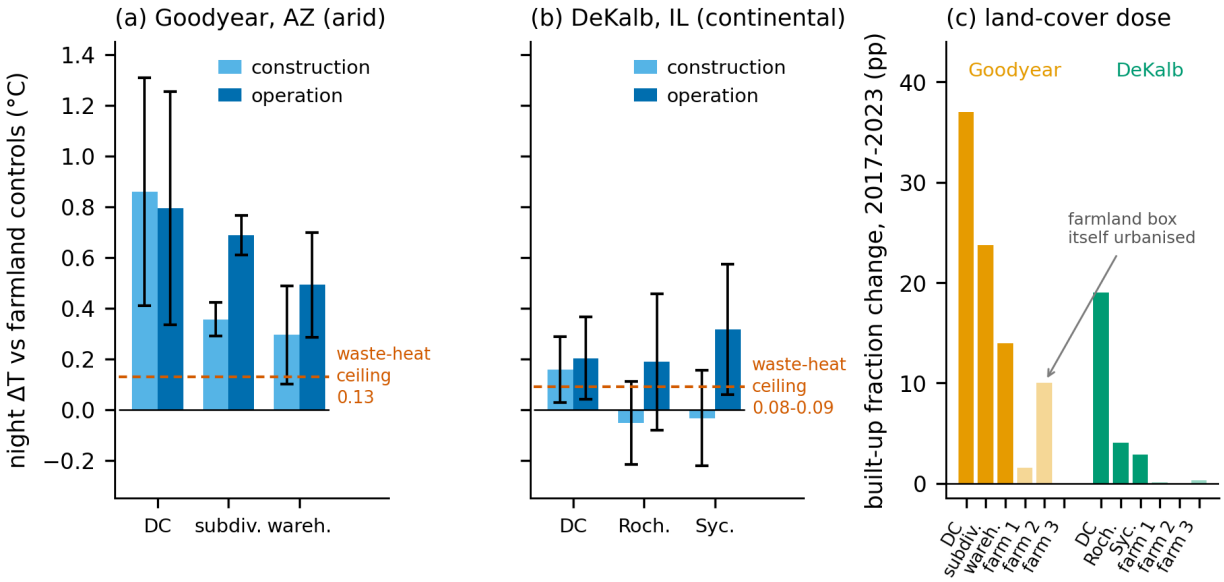


Figure S7. Cross-climate checks of section S5, on the protocol and the month-demeaned convention used throughout. (a) Goodyear, AZ and (b) DeKalb, IL: night-time change from the pre period against the same farmland controls (95% CI), for the data-centre box and the two contemporaneous non-DC development boxes, in the construction and operation phases; the operation phase is the full window in both sites (DeKalb's post-build-out window is reported in the text). Dashed line: the waste-heat ceiling permitted at that site's flux. In both climates the data-centre box's night change is largely in place during construction — before any server load — and is not separable from that of neighbouring development at the power these comparisons afford (~0.4 °C; see the text). (c) Land-cover dose over the product's span: built-up fraction change for the same boxes and for each site's farmland controls (pale). The arid site's ordering is the monotone dose-response described above; the one farmland box that itself urbanised biases its reference warm, against the detected excess. Values reproduced by `scripts/45_figS7_crossclimate.py`, which asserts each of them against the numbers reported in section S5.